Geomorphology 453 (2024) 109148

Contents lists available at ScienceDirect

Geomorphology

journal homepage: www.journals.elsevier.com/geomorphology

Land-surface quantitative analysis for mapping and deciphering the construction processes of piedmont alluvial fans in the Anti-Lebanon Mountains

Giulia Iacobucci [a,*], Michele Delchiaro [a], Francesco Troiani [a], Davide Nadali [b]

[a] Department of Earth Sciences, Sapienza University of Rome, Rome, Italy
[b] Department of Ancient History, Sapienza University of Rome, Rome, Italy

ARTICLE INFO

Keywords:
Piedmont alluvial fans
Anti-Lebanon Mountains
Geomorphological mapping
Fluvial fans
Alluvial fans

ABSTRACT

Land-surface quantitative analysis based on digital elevation model (DEM) has been applied for improving the geomorphological mapping of piedmont alluvial fans. Indeed, these fans are frequently along a mountain front, where a series of coalescing fans may eventually occur. The margins of adjacent fans are rather difficult to map, thus preventing accurate and meaningful quantification of fan morphometric properties such as fan area, length, and slope. These morphometric properties are essential for informing on the influence of climatic conditions and tectonic factors on the fan-building processes. Therefore, in this paper, we propose a quantitative digital mapping approach along a stretch of about 50 km in the southern front of the Anti-Lebanon Mountains. Here, the Geomorphological Map of Syria at 1:1,000,000 scale (1963) reported at least nine piedmont alluvial fans, but these were poorly characterized in terms of geomorphometric characteristics and construction processes. Adopting the 1-arcsec SRTMv3 DEM, we propose a four-step workflow to analyse the feeding catchments morphology and fan morphometry. In this manner, the identification and geomorphological mapping of coalescent piedmont fans as well as the recognition of the main construction process have been improved. The proposed approach can support geomorphological investigations of wide and inaccessible areas—especially where arid and semi-arid climate conditions prevail—as well as where socio-political issues may prevent effective field work.

1. Introduction

Piedmont alluvial fans are key depositional landforms representing the link between the upland sediment source and the downward sink system. These landforms develop when a high-bed load stream passes from an area of high energy to one of reduced stream power, thus depositing a landform typically fan-shaped in plan and wedge shaped in profile (Bull, 1977; Blair and McPherson, 2009; Harvey, 2018) (Fig. 1). The most relevant condition for the alluvial fan development is the transition from laterally confined catchments to open plains where unconfined flows radially spread the sediment without barriers (Ventra and Clarke, 2018). Indeed, the mountain fronts, both on the planet Earth and other planetary surfaces (Harvey, 2005; Radebaugh et al., 2018), are frequently characterized by coalescing alluvial fans.

The coalescence of these landforms represents a key challenge for the geomorphological survey and mapping because their lateral confinement is not always obvious. Furthermore, the formation of these fan-shaped landforms is intricately influenced by variations in climate conditions, tectonics, and human activities. This influence has been discussed by various researchers (e.g., Bull, 1968; Harvey et al., 2005; Stock et al., 2008; Blair and McPherson, 2009; Walstra et al., 2010; Benito, 2013; Macklin and Lewin, 2015; Norini et al., 2016; Karymbalis et al., 2022), thus highlighting the potential for these factors to complicate the morphology and morphometry of such landforms. In fact, the globally recognized role of environmental variability emerges as a fundamental factor in creating disequilibrium conditions in geomorphic systems encompassing hillslopes and interconnected channel networks (Delchiaro et al., 2022).

The geomorphological mapping and characterization of piedmont alluvial fans are quite challenging, but essential for an effective land management and hazard evaluation. Indeed, the main hazard affecting alluvial fans includes inundation by flooding water and/or hyper-

* Corresponding author.
E-mail address: giulia.iacobucci@uniroma1.it (G. Iacobucci).

https://doi.org/10.1016/j.geomorph.2024.109148
Received 1 February 2023; Received in revised form 7 March 2024; Accepted 8 March 2024
Available online 11 March 2024

concentrated solid-liquid flows, which move rapidly with unpredictable paths (Field and Pearthree, 1997). Therefore, the proper geomorphological mapping aimed at representing landforms and their associated processes can be effective for preventing socio-economic losses related to geomorphological hazards (Chelli et al., 2021).

Several qualitative and semi-quantitative field techniques have been developed for discerning coalescent fans (e.g., McFadden et al., 1989) requiring time and resources. However, the combination of field surveys and photointerpretation of both aerial and satellite images is the most common technique for the fan identifications and mapping (Crouvi et al., 2006). Recently, remote sensing tools like image processing in combination with geomorphometry can classify different types of fans even when our knowledge of field conditions is scarce (Babič et al., 2021). Although the exclusive use of remotely sensed data for producing geologically plausible predictions is, in general, quite challenging (e.g., Weiss and Walsh, 2009; Cracknell and Reading, 2014; El Fels and El Ghorfi, 2022), the development of innovative techniques allow it to considerably support geomorphological investigations over inaccessible and wide territories (Knight et al., 2011; Verstappen, 2011; Iacobucci et al., 2020, 2022a, 2022b).

Considering the extent of the piedmont alluvial fans, we propose here a land-surface quantitative analysis using open access DEM data. This approach aims to (i) map the limit of coalescent fans in the piedmont area, and (ii) determine the main construction process considering the morphometry of both fans and feeding catchments, discerning between alluvial and fluvial fans by specific morphometric parameters (Ventra and Clarke, 2018; Harvey, 2018). Alluvial fans (AFs) have i) small feeding catchments with high relief; ii) short radii (hundreds of meters up to few kilometres); iii) high slopes; and iv) the prevalence of runoff events of relatively short duration (e.g., debris flows and hyperconcentrated flows). On the other hand, fluvial fans (FFs) present i) wider surfaces with radii of tens up to hundreds of kilometres, ii) low slopes, iii) extensive and well-integrated feeding catchments, and iv) the prevalence of fluvial processes (Ventra and Clarke, 2018; Harvey, 2018; Moscariello, 2018).

The southern margin of the Anti-Lebanon Mountains (ALM), in the southwestern sector of Syria, is an ideal study area where several alluvial fans with different sizes and shapes, but poorly studied in literature, crop out. Moreover, the application of a remotely desk geomorphological approach is favoured by the absence of vegetation and is potentially suitable for refining the planar fan shape and boundaries, as well as for supporting the assessment of the main construction processes responsible for the fan's genesis and development. Therefore, we propose here a four-step workflow where morphometric and non-morphometric parameters of both feeding catchments and fans have been collected, analysed and clustered.

2. Study area

The study area is located at 33°20′00″ to 33°50′00″ N and 35°55′00″ to 36°45′00″ E between the intermontane continental basin of Damascus (i.e., Damascus Basin) and the ALM (Fig. 2). The entire study area is about 4300 km^2 where more than 50 % of the western and northern sector is mountainous with elevation between 1200 up to 2800 m a.s.l. The southeastern sector presents a low relief ranging between 600 and 1100 m a.s.l. Considering the extent of the study area, the climatic

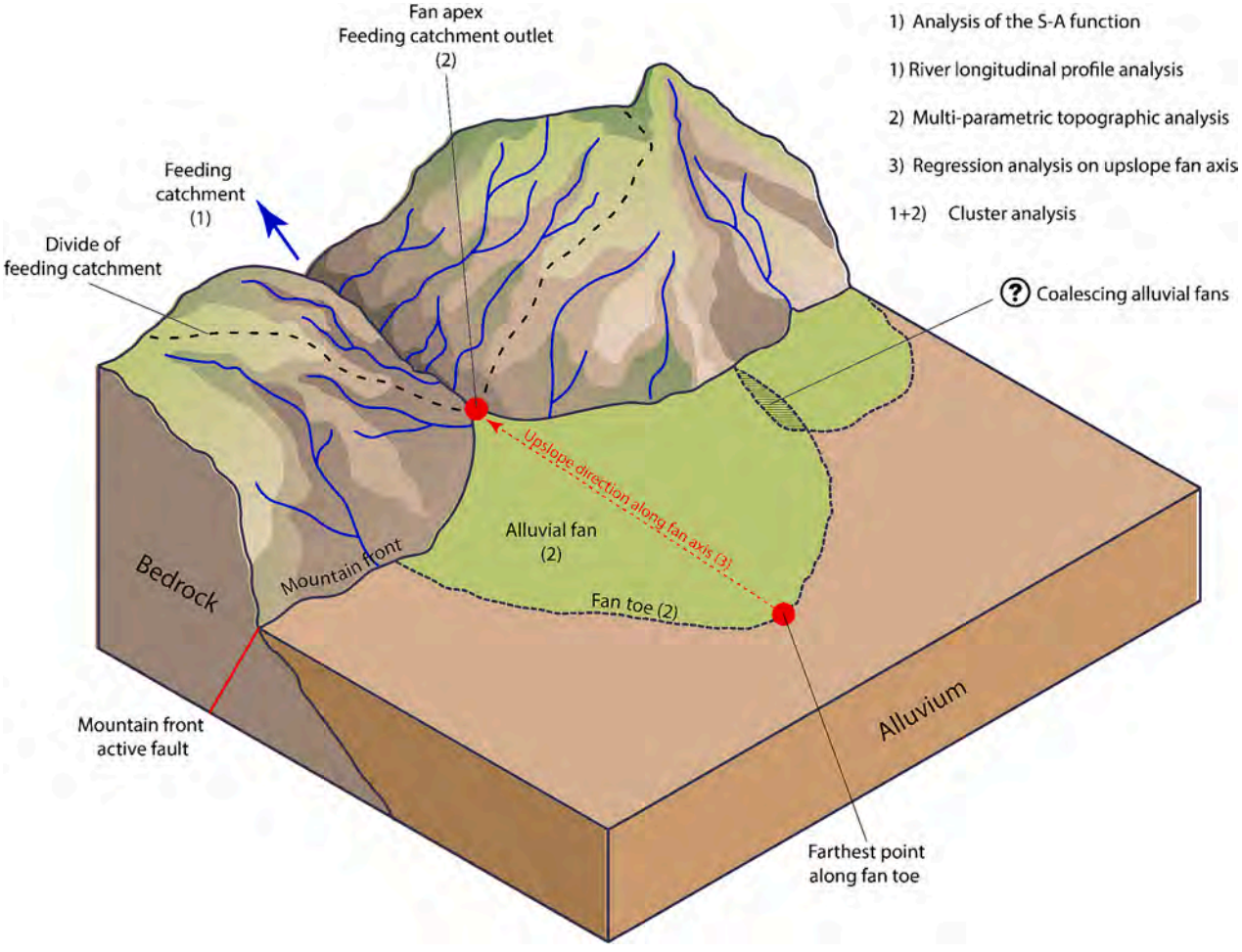

Fig. 1. Cartoon sketch of the piedmont alluvial fans. The numbers in brackets show the fan elements considered in each analysis of the workflow.

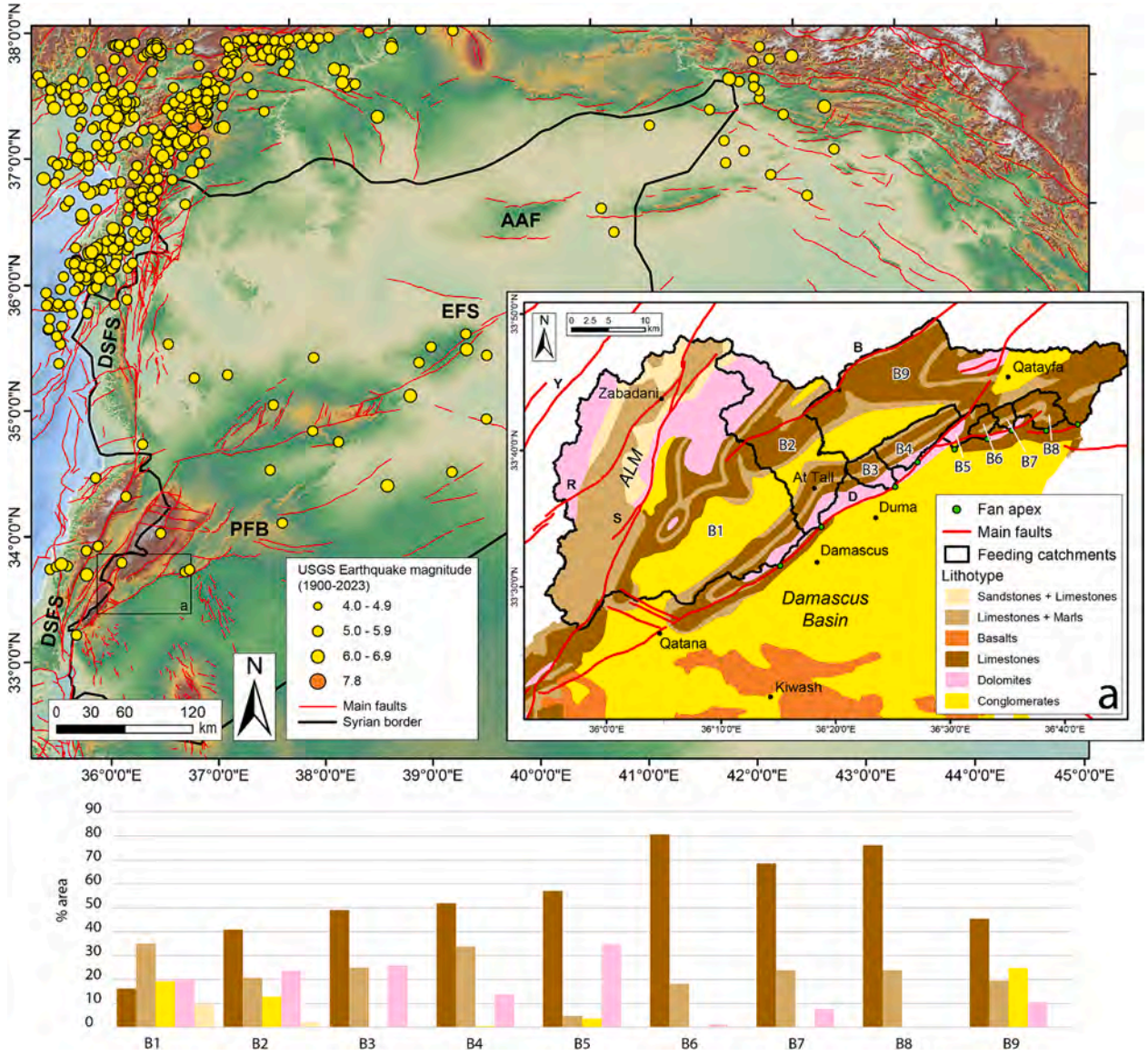

Fig. 2. Map showing the location of the study area (black rectangle) between the intercontinental Damascus Basin and the ALM, in relation to the Syrian tectonic zones and the historical earthquakes (https://earthquake.usgs.gov/earthquakes/map/): DSFS (Dead Sea Fault System), PFB (Palmyra Fold Belt), EFS (Euphrates Fault System), and AAF (Abdel-el-Aziz Faults). a) The lithological map derived from the Geological Map of Syria (1964, https://exhibits.library.cornell.edu/barazangi-map-collection/catalog/60-2733) with the main faults of the study area: Y (Yammouneh fault), R (Rachaya fault), S (Serhaya fault), B (Bassimeh fault), and D (Damascus fault). The mapped faults derive from the Active Faults of Eurasia Database v2022 (Zelenin et al., 2022). Histograms showing the percentage of the lithotypes outcropping within each analysed catchment (i.e., B1 to B9 from west to east) are reported.

setting is quite heterogeneous, distinguishing three main climatic regions: the Mediterranean one in the ALM (Csa), the semi-arid region in the easternmost sector (BSk), and the arid region in the Damascus Basin (BWk) (Fig. 3). Indeed, the western mountainous sector represents a precipitation barrier, which progressively decreases the rainfalls eastward (Kattan, 2006; Zepner et al., 2020; Baba et al., 2021).

The Syrian region is crossed by four tectonic zones as shown in Fig. 2: the Dead Sea Fault System (DSFS), the Abd-el-Aziz Faults (AAF), the Euphrates Fault System (EFS), and Palmyra Fold Belt (PFB) (Barazangi et al., 1993; Brew et al., 2001; Abdul-Wahed, 2022). The study area is between the DSFS and the southwestern margin of the PFB, where several active faults are recognized like the Damascus and Bassimeh reverse faults as well as the Serghaya and Rachaya left-lateral faults (Brew et al., 2001; Kattan, 2006; Abou Romieh et al., 2012) (Fig. 2a). According to Abou Romieh et al. (2012), the Damascus fault has a throw of about 2500 m, while the Bassimeh fault of approximately 1000 m. These faults became active around 0.9 Myr, with estimated vertical slip rates of about 1.1 mm y^{-1} for the Bassimeh fault and 2.8 mm y^{-1} for the Damascus fault. The Authors explained the lack of major earthquakes and low slip rate recently measured geodetically in the area (Alchalbi et al., 2010) due to crustal shortening within the region.

The lithological units derived from the Geological Map of Syria (1964) (Fig. 2a) show that limestones and limestone/marl alternations mainly occur in the mountain sector, while the intermontane basins are characterized by conglomerates. Specifically, the widest basins at B1, B2, and B9 are characterized by a greater lithological heterogeneity than the smallest ones (B3-B8). Generally, the outcropping lithologies within basins are quite homogeneous in terms of erodibility—primarily consisting of limestones and limestone/marl alternations. As reported in the Geomorphological Map of Syria at 1:1,000,000 scale completed in 1963 (https://esdac.jrc.ec.europa.eu/content/geomorphological-map-syria), the southeastern piedmont sector of the ALM is essentially characterized by several Quaternary alluvial deposits mapped as alluvial fans and developed in a flat saline plain. The catchment area is characterized by

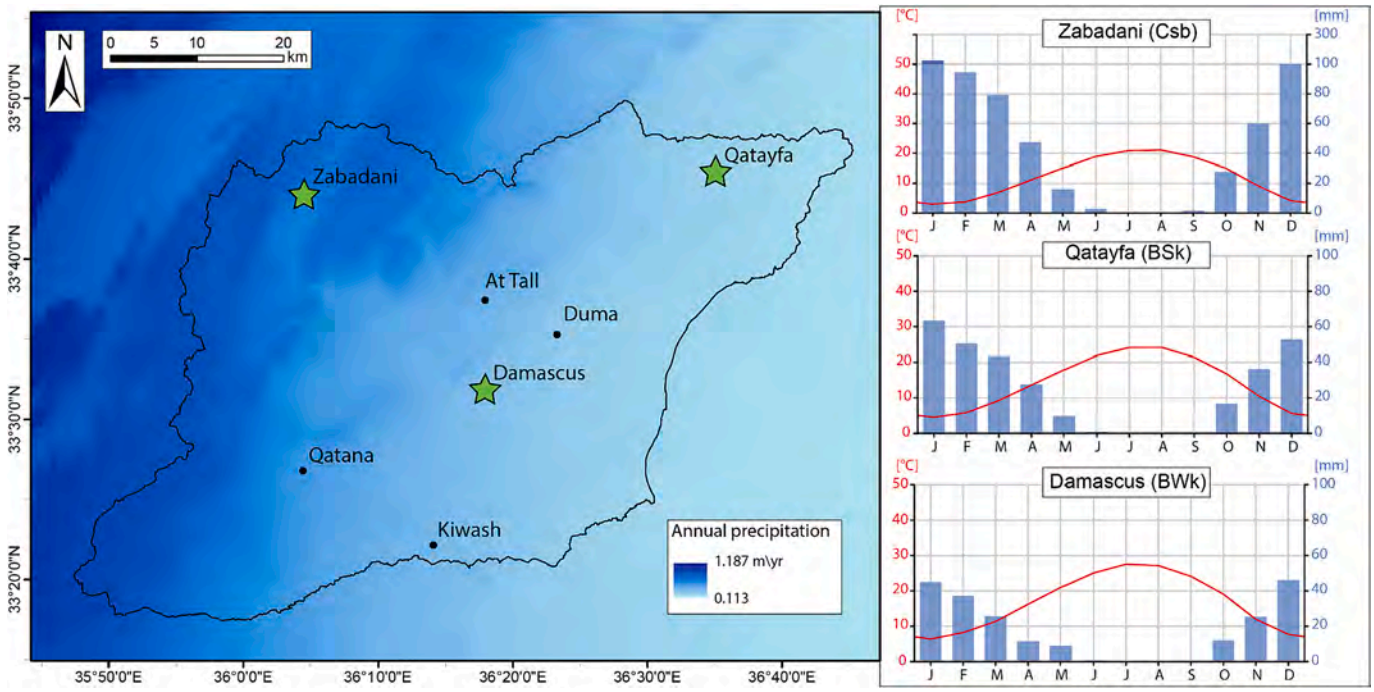

Fig. 3. The mean annual precipitation extracted from WorldClim version 2.1 (Fick and Hijmans, 2017) with data collected from 1970 to 2000. The green stars represent the location of the climate charts reported on the left.

folded mountains. Specifically, the western sector corresponding to B1 and B2 was distinguished in medium - height mountains with flattened divides and steep slopes as well as low mountains with small and low ridges. The eastern sector (B9) has low mountains with coniform and cuesta-hilly relief. Finally, the area proximal to the Damascus fault, where smallest catchments have been delineated, were classified as mountains of medium height with narrow divides and longitudinal valleys (Geomorphological Map of Syria at 1:1,000,000 scale, 1963).

3. Materials and methods

The present section provides information about the adopted materials and the methodological approach based on quantitative analyses of land-surface topography. The diagram in Fig. 4 summarizes the research workflow, specifying each step of the proposed analysis that will be detailed in dedicated sub-sections. Specifically, adopting the 1-arcsec SRTMv3 DEM, we propose i) the analysis of the total-basin slope-area function to extract the drainage network and delineate fluvial process domain (Vergari et al., 2018) as well as to estimate the rainfall contribution to its spatial distribution; ii) the analysis of the longitudinal profiles of the extracted drainage network in each feeding catchment to understand the tectonic influence on fan development; iii) the multi-parameter topographic analysis (sensu Piacentini et al., 2021; Iacobucci et al., 2022a, 2022b) to improve the mapping of fan boundaries; iv) the application of a regression analysis to the upslope profiles of the fan axis (sensu Williams et al., 2006) to support the interpretation of the fan construction process; and v) the computation, assessment, and clustering of selected parameters of both feeding catchments and alluvial fan bodies to identify the cluster tendency and to investigate the catchment-fan relationship.

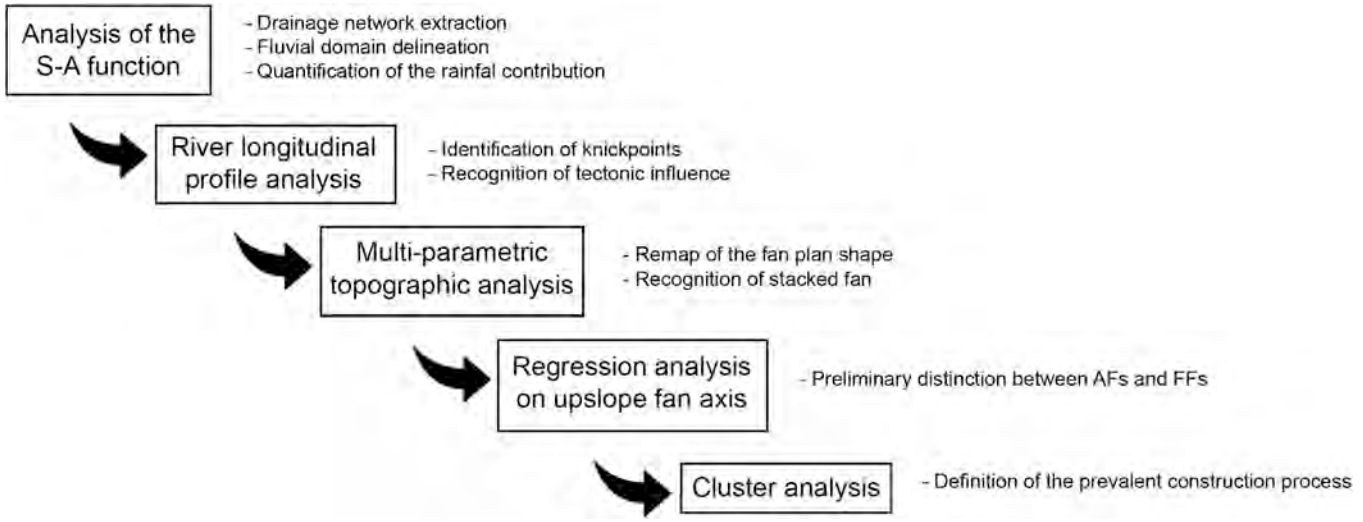

Fig. 4. The workflow with the main steps (black rectangles) and the specific outputs.

3.1. Analysis of the slope-area (S-A) function

Given the inherent connection between the formation of alluvial fans and the morphological characteristics of their feeding catchments, as well as the gradients in rainfall distribution, we first focused the analysis on the drainage basins situated upstream of the fan apex points. Our objective was twofold: first, to ascertain the flow accumulation that initiates the fluvial domain delineating the predominant processes in the feeding catchments; and second, to quantify the impact of spatial rainfall gradients. This entailed the computation of the total-basin slope-area (S-A) function wherein both the flow accumulation weighted and unweighted by the precipitation rate were considered for each catchment under investigation.

In the S-A analysis, the slope S (m m^{-1}) can be empirically expressed as a function of the drainage area A (m^2) computed for each pixel of the drainage basin (e.g., Vergari et al., 2018; Delchiaro et al., 2023). Generally, the relationship between S and A is positive at low A values, but the slope of the curve becomes negative for higher A values suggesting a more fluvial domain (Vergari et al., 2018 and reference therein). Subsequently, to quantify the influence of spatial rainfall gradients on single catchments, the S-A function was also computed with the flow accumulation weighted by the precipitation rate R (m yr^{-1}), approximated by the stream discharge (A•R, m^3 yr^{-1}) according to Adams et al. (2020). With this approach we can derive two different drainage networks: one unweighted and the other weighted by the precipitation rate.

The drainage network has been extracted from the SRTM version 3 DTM (SRTMv3) using the TopoToolbox (Schwanghart and Scherler, 2014). The selected DTM was generated in 2000 and downloaded from the US Geological Survey's EarthExplorer website. Its ground resolution is 1 arcsec (specifically 29.10 m in the study area), with an expected vertical accuracy of about ±16 m absolute and ± 6 m relative (Mukul et al., 2017; Elkhrachy, 2018; Uuema et al., 2020). As reported by several authors (Boulton and Stokes, 2018; Woor et al., 2023), the ALOS World 3D-30 m (also known as AW3D30) DEM is the best for analysing landforms and processes due to superficial running waters in highland areas. However, several anthropic noises have been detected, especially in the westernmost sector of the Damascus Basin, so the adoption of AW3D30 was prevented.

3.2. River longitudinal profiles analysis

To comprehend the tectonic influence on fan development, we conducted an analysis of river longitudinal profiles. Longitudinal profiles retain important characteristics, including non-lithological knickpoints that signify variations in rock uplift rates, reflecting changes in base level (Delchiaro et al., 2021; Expósito et al., 2022; Pirrotta et al., 2022; Moumeni et al., 2024). The stream network utilized for this analysis was derived through the application of a flow accumulation threshold for initiating the fluvial domain. The identification of knickpoints was achieved using the *knickpointfinder* function of TopoToolbox (Schwanghart and Scherler, 2014; Stolle et al., 2019), with a tolerance height value set at 30 m.

3.3. Multi-parameter topographic analysis on radial profiles

The alluvial fans mapped in the Geomorphological Map of Syria at 1:1,000,000 scale (V/O Technoexport, 1963) have been considered in this step starting from the evaluation of the fan apex position aligned to the catchment outlets of B1-B9. We next considered three elements to

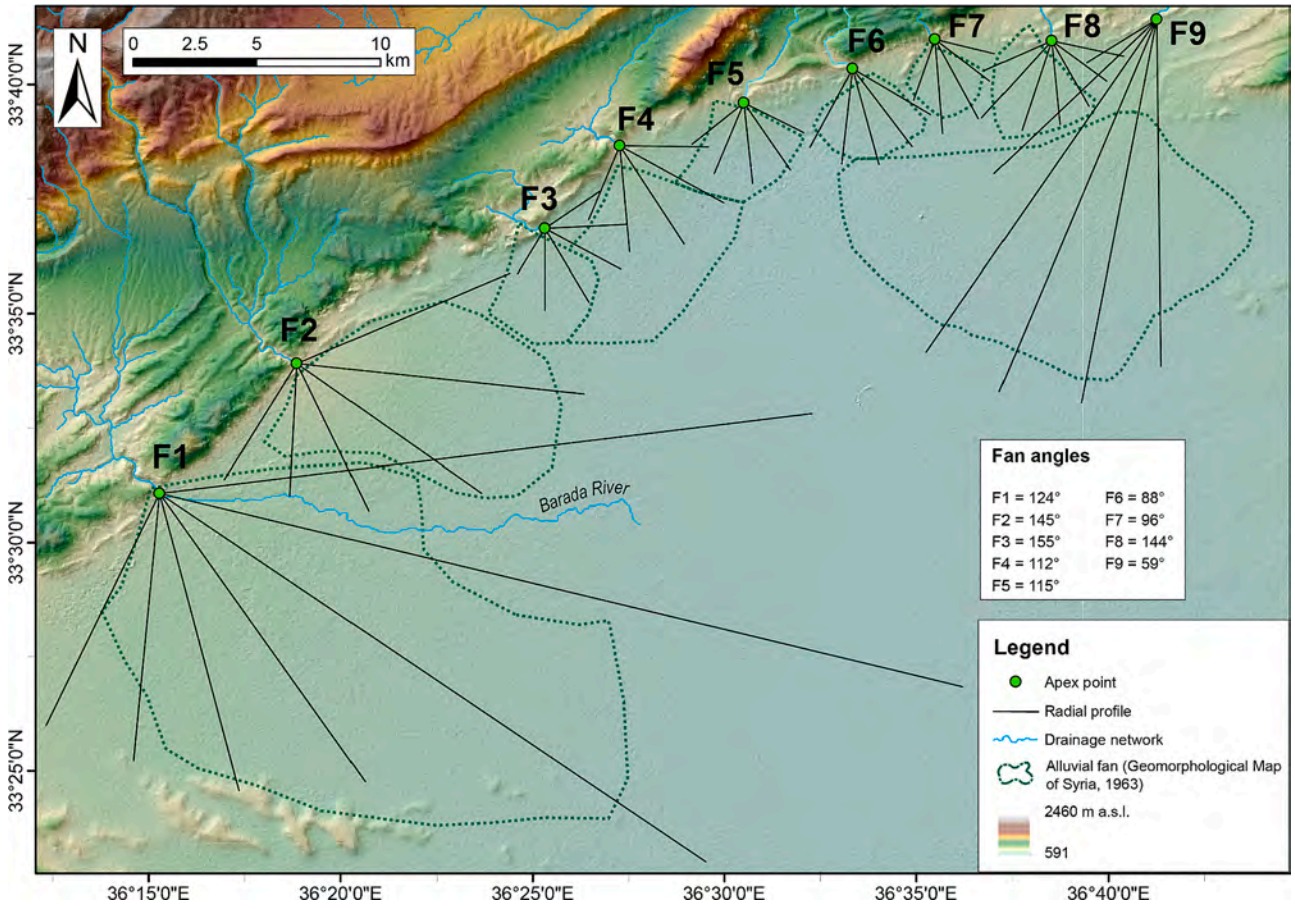

Fig. 5. The radial profiles made for each fan (F1-F9) with apex points marked by green points.

recognize and remap the exact plan shape of the nine fans (F1-F9; Fig. 5): i) the elevation of fan apex/catchment outlet; ii) the commonly conical shape; and iii) the "sope-break" between the mean slope of the fan surface and the adjacent valley floor typically along the fan toe (Norini et al., 2016). The landforms reported in the Geomorphological Map of Syria and the extracted contour lines from the SRTMv3 DEM are landmarks for drawing a series of radial profiles starting from the fan apex up to the distal sector. This also includes the area beyond the fan toe (Williams et al., 2006; Norini et al., 2016). The radial profiles were drawn considering the maximum angle within which each fan is included (59° for the narrowest F9 up to 155° of F3) and splitting these angles to have at least five profiles for each fan (Fig. 5).

The position of the fan toe along the radial profiles is determined considering the terrain elevation and the mean slope of the profile (Norini et al., 2016). To recognize the "slope-breaks", we considered the slope as the most suitable morphometric parameter that can detect the distal sectors. Precisely, when the values of the slope along the profiles are above the first standard deviation (σ) or the mean (μ), we can identify the topographic signature of the detected landform (Iacobucci et al., 2022a, 2022b) (for example Figs. 8, 9, and Supplementary materials 1).

3.4. Regression analysis on upslope fan axis

Once the distal end points were recognized along each radial profile and the fan distal edges were correctly mapped, we next plotted the slope vs upslope distance computed along the fan axis. Williams et al. (2006) represented the fan shape by plotting the slope as a function of the distance given that the slope is independent from the location along the fan axis. We applied a moving average filter for smoothing the sampling data with a sliding window of length 5 or 10 for the smallest (F3-F8) and largest fans (F1/F2/F9), respectively. The regression analysis of the slope vs upslope distance plots were performed using the exponential and the power law regressions as proposed by Williams et al. (2006). The selection of the resulting exponential vs power law model was performed by considering the coefficient of determination R^2. In fact, according to Williams et al. (2006), the AFs are characterized by greater slopes and shorter fan axis than FFs, with the slope values progressively increasing in the apex sector. Resulting in a more concave-up profile, it should be better described by an exponential model in the regression analysis. In contrast, the FFs profile is characterized by lower slopes that constantly increase toward the apex sector, and the power law model is the most suitable.

3.5. Cluster analysis

To investigate the relationships between the morphometric and non-morphometric parameters describing both the fans and the corresponding catchments—as well as the clustering tendency between AFs and FFs—the *k-means* cluster analysis available in the open-source software JASP 0.16.4.0 (JASP Team, 2023 - JASP version 0.17 Computer Software) was applied. *K-means* clustering is a hard partitioning algorithm that aims to partition data into several clusters, where each observation belongs to only one group. The data is divided such that the degree of similarity between two data observations is maximal if they belong to the same group and minimal if not. We used MacQueen's algorithm setting the centre type as "means", 25 as maximum number of iterations, and 25 as maximum number of possible random sets used. Moreover, the cluster determination was optimized according to Bayesian Information Criterion (BIC) obtaining 2 clusters.

The morphology and morphometry between AF and FF are rather different, and thus we selected 13 parameters (Table 1), many of which have been already proposed in previous works (e.g., Santangelo et al., 2012; Mokarram et al., 2014; Karymbalis et al., 2016; Karymbalis et al., 2022; Özpolat et al., 2022; Woor et al., 2023). The study of these parameters can be useful for predicting the prevailing process such as erosion or deposition (Mokarram et al., 2022), and then deducing the main depositional process (Santangelo et al., 2012). Among the selected parameters, Melton's roughness index (C_{mr}) can potentially discern between AF and FF, thus discriminating between different transport processes (e.g., Kostaschuk et al., 1986; Crosta and Frattini, 2004; Karymbalis et al., 2016). In addition to the morphometric parameters, we also considered the mean annual precipitation of each catchment (C_p). The latter can play a relevant role, especially in the smallest basins that are more sensitive to extreme events. The channel length of each feeding catchment was computed considering the unweighted drainage network because it matches with the TerraColor satellite images.

Finally, we evaluated which parameter is more significant in the distinction between AF and FF, thus allowing us to surely define the prevailing construction process.

Table 1
The morphometric parameters considered for discerning AF and FF.

Parameter	Abbreviation	Units	Description
Fan			
Area	F_a	km^2	Planimetric area of fan
Slope	F_s	m m^{-1}	Axial slope from apex to toe
Length	F_l	km	Axial length from apex to toe
Apex elevation	F_{ae}	m a.s.l.	Elevation of fan apex above sea level
Toe elevation	F_{te}	m a.s.l.	Elevation of fan toe above sea level
Relief	F_r	m	Difference in fan elevation from the apex to the toe
Catchment			
Area	C_a	km^2	Planimetric area of the catchment above the fan apex
Total channel length	C_{cl}	km	Total length of channels within catchment
Drainage density	C_{dd}	–	Ratio of total length of channels to total area of catchment
Circularity index	C_{ci}	–	Derived by the equation Circ = $4\pi Ac/Pc^2$ that expresses the shape of catchment
Relief	C_r	m	Vertical difference between maximum catchment elevation and fan apex elevation
Melton's roughness index	C_{mr}	–	Change in catchment relief across space: $C_{mr} = C_r * C_a^{-0.5}$ (Melton, 1965)
Mean annual precipitation rate	C_p	m yr^{-1}	Available at https://www.worldclim.org/data/worldclim21.htm

4. Results

4.1. Analysis of the S-A function

Fig. 6 reports the S-A functions with the flow accumulation weighted and unweighted by the precipitation rate related to the entire catchments area as well as to the single catchments. A minimum drainage area of 1.5 10^6 m^2 and a minimum discharge of 10^6 m^3 yr^{-1} were obtained for the channel initiation from the entire area curves (Fig. 6a), based on the computation of the slope derivative (dashed lines in Fig. 6a) of the S-A function, as suggested by Vergari et al. (2018).

By juxtaposing the trends of the curves (Fig. 6b) and examining the maximum values at the apex points (Fig. 6c) associated with individual catchments, the difference between the two curves and the maximum values is gradually greater from B1 to B8. This underscores the impact of decreasing rainfall from B1 to B8. In contrast, B9 exhibits a comparatively smaller difference in both curve trends and maximum values.

However, it is also possible to observe a strict dependence between the spatial distribution of the fluvial process domain and the size of the

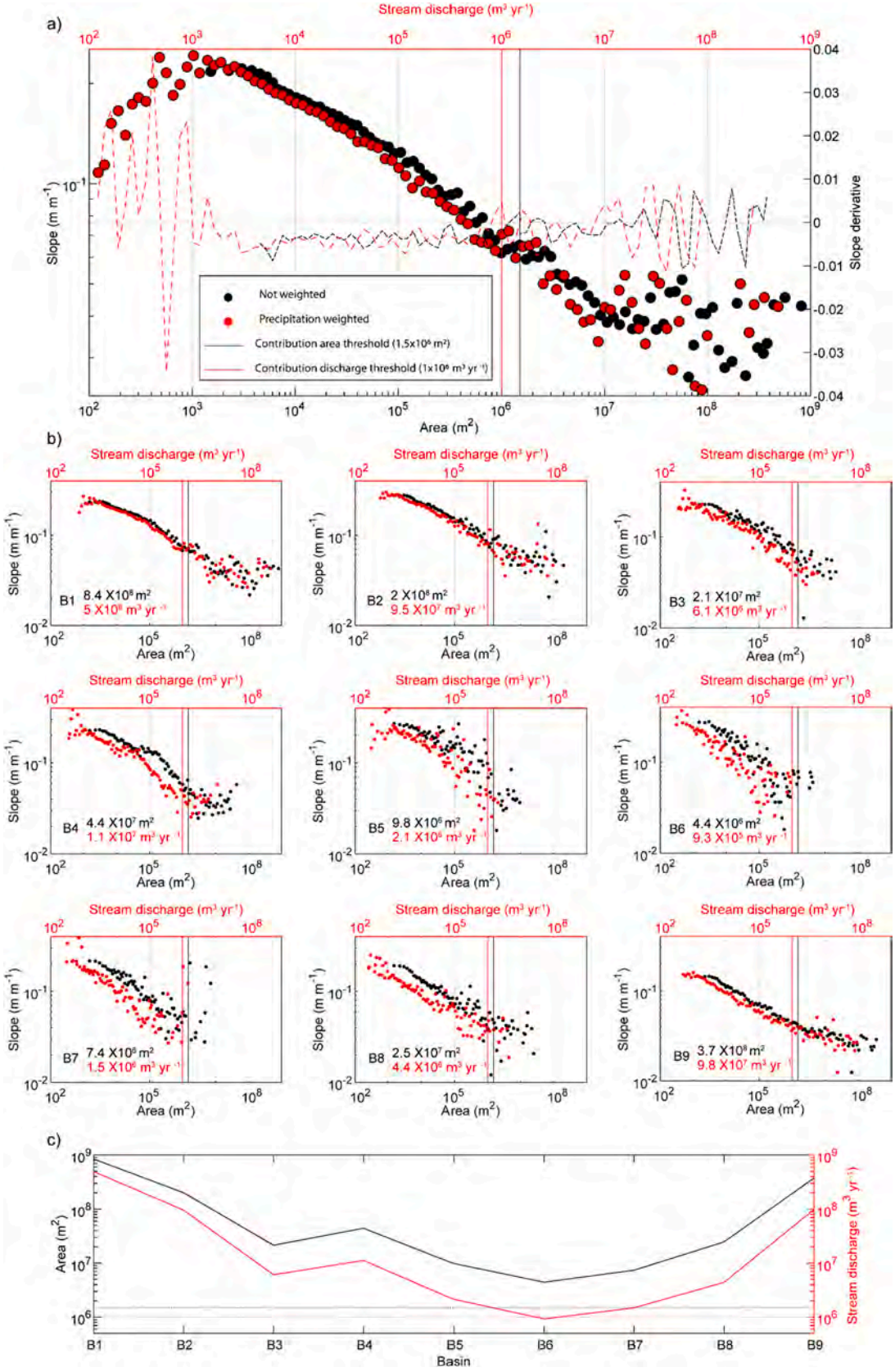

Fig. 6. a) The total-basin S-A functions with the flow accumulation weighted and not weighed by the precipitation rate related to all the catchment areas for the fluvial domain thresholds delineation. The slope derivatives are also reported as red and black dashed lines, respectively for weighted and not weighed cases. b) The total-basin S-A functions for the single feeding catchments (B1–B9). c) The maximum values of contributing area and stream discharge versus the thresholds.

catchment in Figs. 6c and 7. Notably, there is a consistent decrease in the values of the contributing area from B1 to B6, ranging from nearly 10^9 m^2 to just below 10^7 m^2. Subsequently, the values rebound from B7 to B9. All values remain above the 1.5 10^6 m^2 threshold defined for the fluvial domain. Nevertheless, it is interesting to observe that the stream discharge at the apex point for basin B6 marginally falls below the 10^6 m^3 yr^{-1} threshold, thus indicating that the fluvial processes are not developed at all (Fig. 6c).

4.2. River longitudinal profile analysis

As we can already observe in Fig. 7, the weighted and unweighted drainage networks are considerably different in length, especially in the easternmost basins (B5-B9). Furthermore, in order to cross-check the morphological imprint of the drainage network, we have compared both drainage networks to TerraColor Satellite images in ArcGIS 10.8.2 (https://hub.arcgis.com/datasets/esri::world-imagery/about). The extracted drainage networks present a rectangular pattern, especially in the largest basins where several stream piracy can be deduced. Moreover, by examining the longitudinal profiles of the rivers shown in Fig. 8, it becomes evident that knickpoints are present exclusively within basins B1, B2, B7, and B9. Among these, the most significant knickpoint heights are observed solely within basins B1 and B2. In contrast, basins B7 and B9 exhibit one knickpoint with a height of 87 m and three knickpoints ranging from 33 to 38 m in height, respectively.

4.3. Multi-parameter topographic analysis

Five to seven radial profiles were computed for each fan (52 in total), and the identified "slope-break" points were mapped as end points. The radial profiles of the largest fan F1 and the smallest one F3 are reported here as examples (Figs. 9, 10, and 11). The other ones (F2, F4-F9) are available in the Supplementary materials 1.

The profiles of F1 show the eastward development of the deposit because the mapped end points are about 20–30 km from the apex point along the profiles p5-p7. The area of F1 is about 358.8 km^2 (Fig. 9a), which is greater than the mapped fan in the Geomorphological Map of Syria. The apex point is 706 m a.s.l., taken in the Barada river channel, but the elevation of several points is greater than 700 m—especially where local reliefs occur (e.g., p1 of F1 in Supplementary materials 1) and where the Barada's levees are evident (e.g., p1-p3 of F1 in Supplementary materials 1). Fig. 10 shows the most significant profiles (p4, p5, p6, and p7), where specific characteristics can be observed. In each profile, at least three different zones can be recognized (similarly to the profiles of F9 in Supplementary materials 1): the first one is characterized by slope values greater than the first standard deviation (σ), the second one presents the slope values between the mean (μ) and the first standard deviation, and the last one has slope values below or proximal to the mean, thus remaining quite steady. Only along profile p7 can we distinguish four different zones, i.e., a more convex shape is seen between 3 and 13 km.

The smallest fan F3 is only 6.4 km^2 (Fig. 9b) with a regular shape. Its deposit in the Geomorphological Map of Syria is not clearly mapped, but its presence is confirmed by the radial profiles and the extracted contour lines. The slope-breaks recognized as end points are about 2 km from the apex point, where the topographic expression of the plain is marked by slope values below or proximal to the mean values. Conversely, the fan deposit (i.e., from the apex to the end points) is characterized by slope values above the first standard deviation (Fig. 11). The apex point has been extracted along the feeding channel at the outlet point of the catchment (690 m a.s.l.), but the radial profiles do not show topographic evidence of the drainage system as in F1.

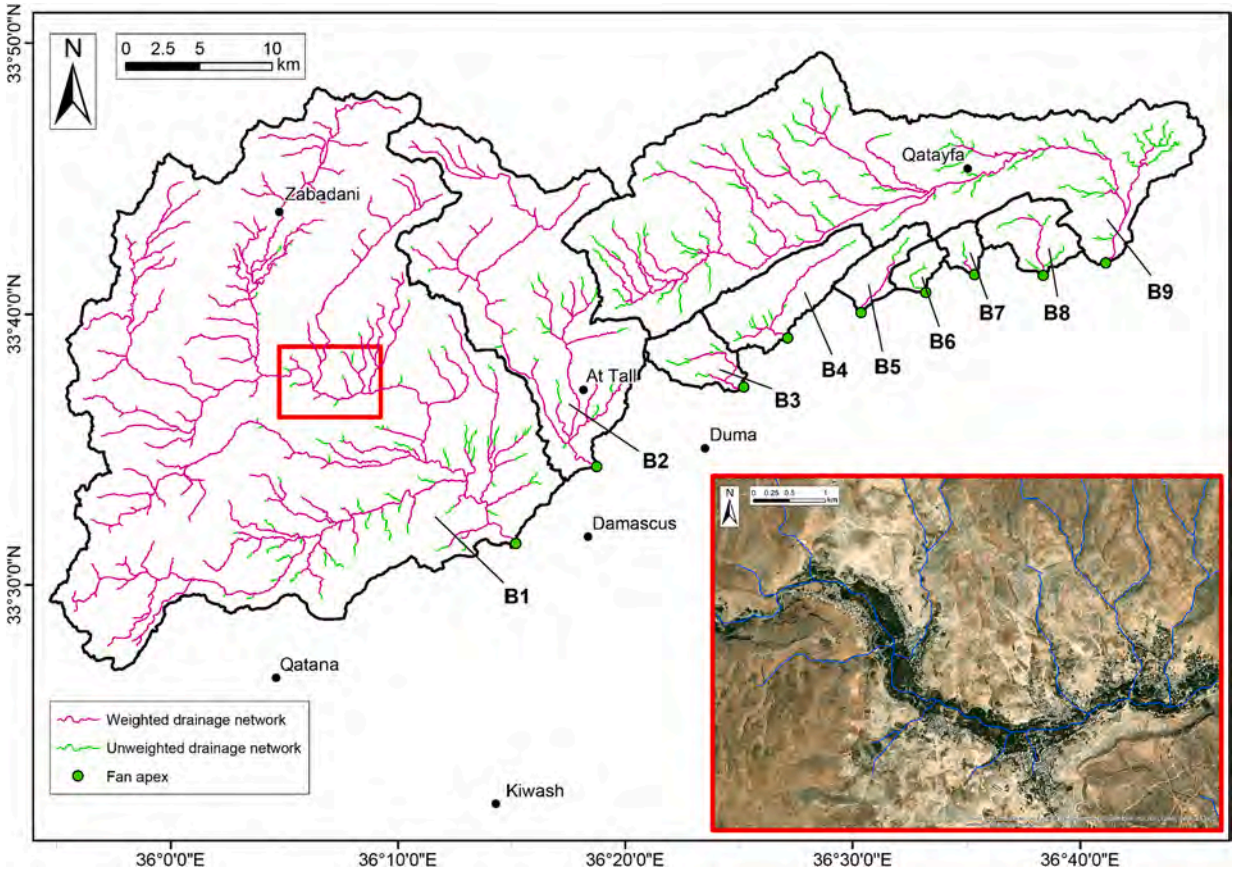

Fig. 7. The extracted drainage network in the nine feeding catchments (B1–B9) and the knickpoints. The red rectangle shows a detail of the TerraColor images where the extracted drainage network (unweighted) matches up with the satellite view.

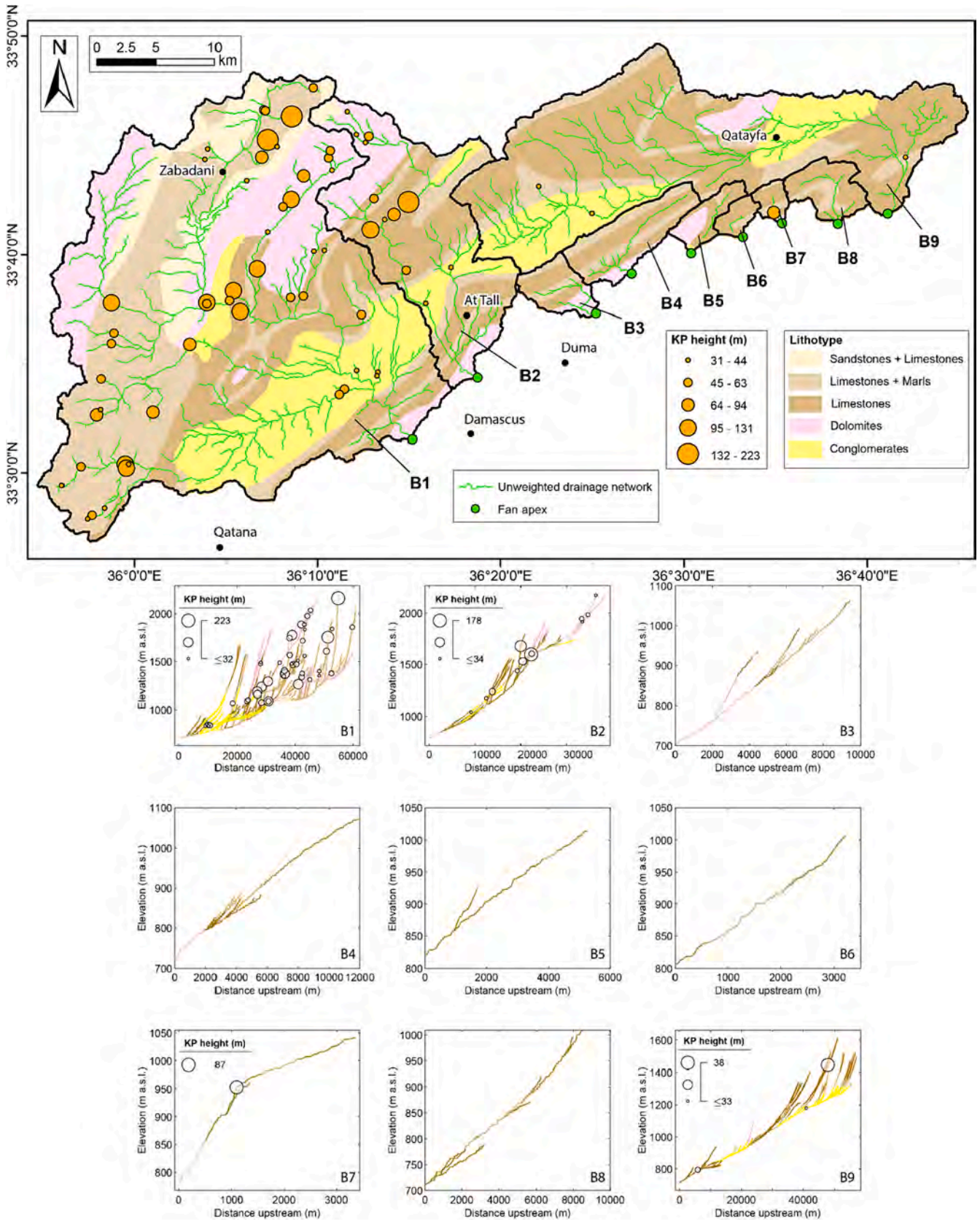

Fig. 8. The location of knickpoints along the unweighted drainage network in B1–B9 basins, and the longitudinal profiles of upstream stream networks with identified knickpoints. Additionally, the corresponding lithology intersected by the profiles is indicated.

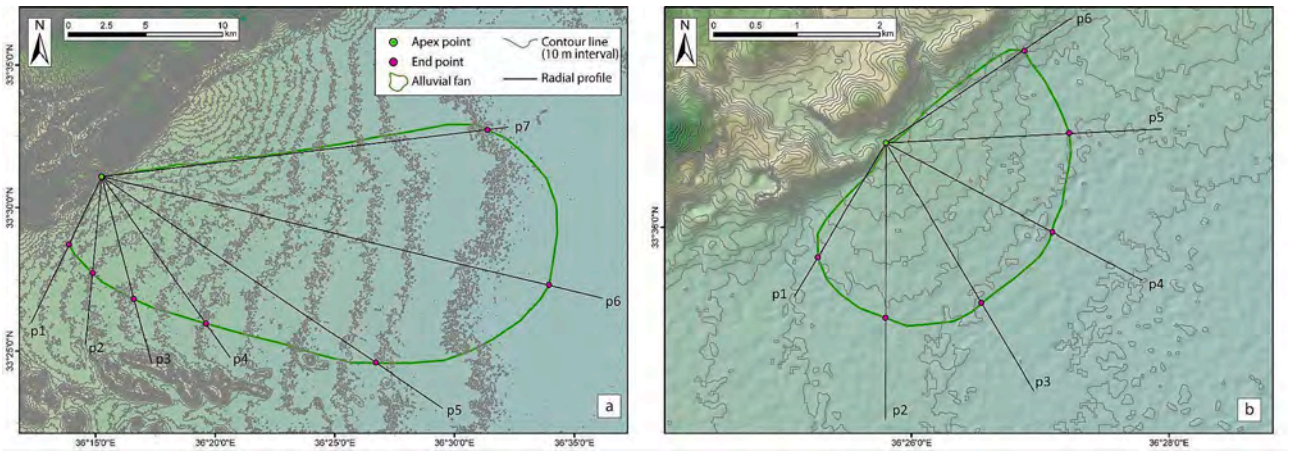

Fig. 9. The radial profiles of the largest fan F1 (a) and the smallest fan F3 (b).

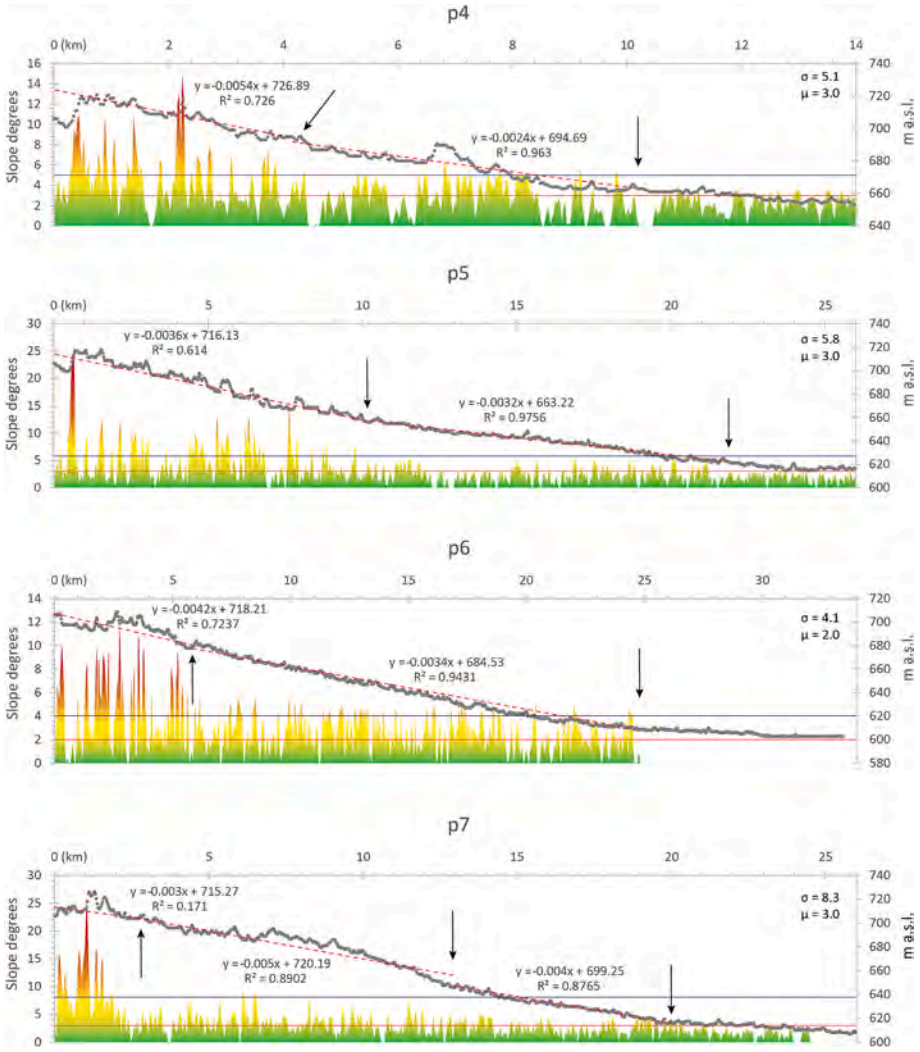

Fig. 10. The radial profiles (dotted grey lines) of F1 where the evidence of "slope-breaks" along p4, p5, and p6 are pointed out by the black arrows. The slope color bar is helpful for discerning the fan from the alluvial plain: red values above the first standard deviation and yellow values above the mean detect the fan, while green values below the mean detect the alluvial plain beyond the fan toe. The recognition of different sectors are evident considering the linear regression (dotted red lines). The intersection of the convex longitudinal profile of F2 is evident between 3 and 13 km in profile p7. The horizontal blue and red lines represent the first standard deviation (σ) and the mean (μ) of the slope, respectively.

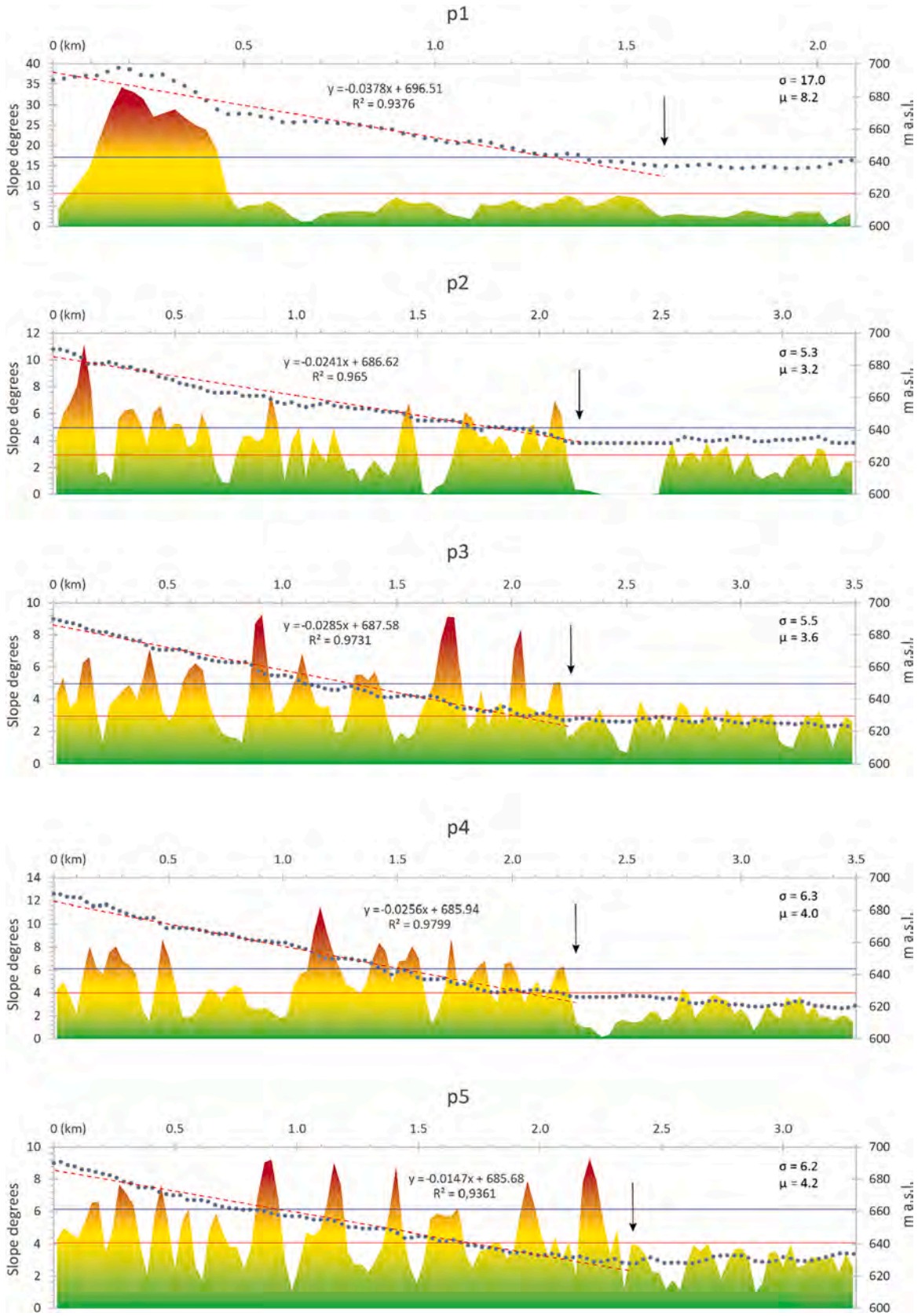

Fig. 11. The radial profiles of F3 (except for p6 are available in Supplementary materials 1) are represented by dotted grey line; the black arrows indicate the recognized "slope-breaks" along the fan deposit and mapped as end points. The slope color bar is useful for distinguishing the fan from the alluvial plain: red values above the first standard deviation and yellow values above the mean detect the fan, while green values below the mean detect the alluvial plain beyond the fan toe. The distinction between fan and alluvial plain, and the identification of the "slope-breaks" are evident in the linear regression (dotted red lines). The horizontal blue and red lines represent the standard deviation (σ) and the mean (μ) of the slope, respectively.

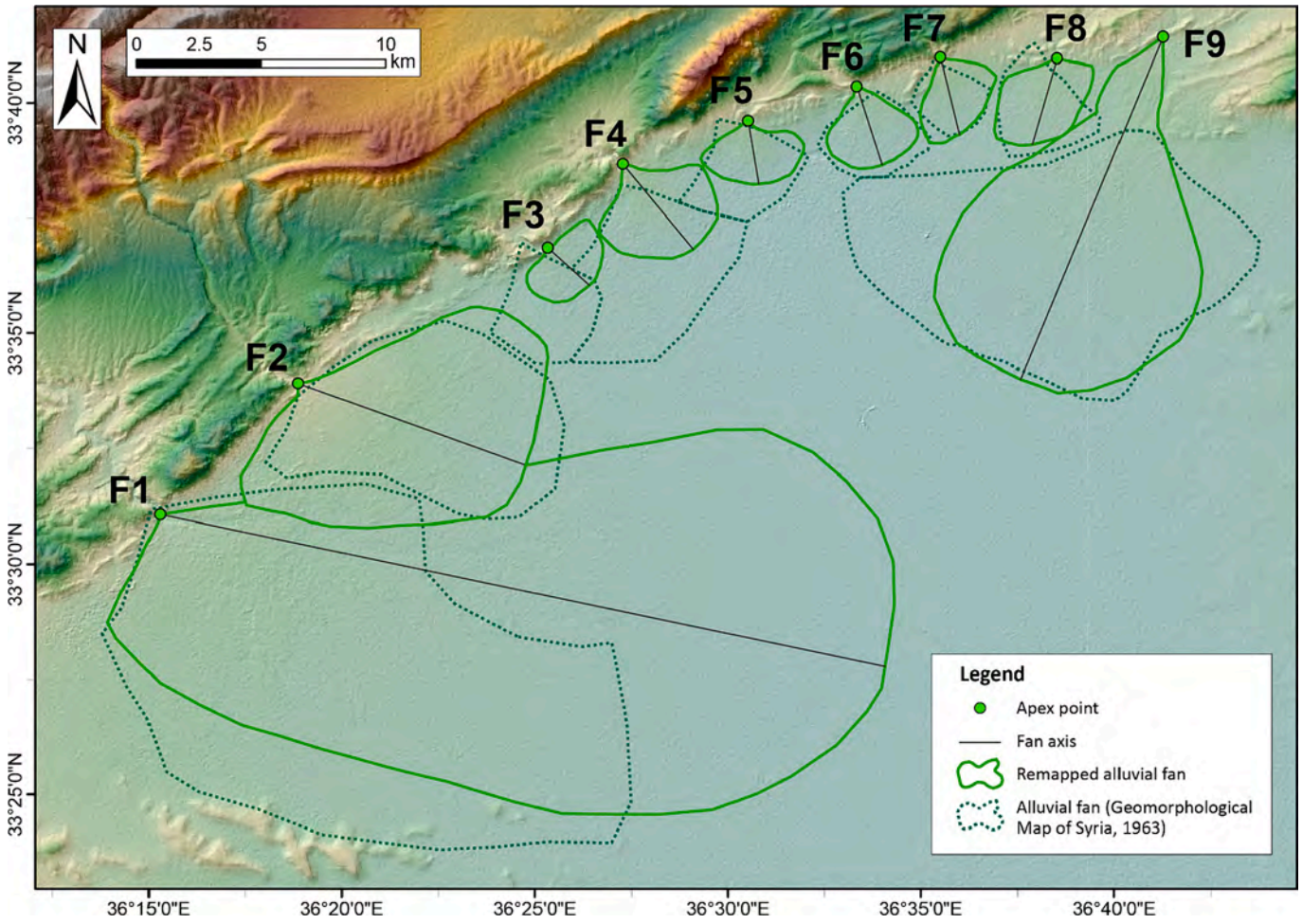

Fig. 12. Remapped alluvial fan shapes F1–F9 thanks to the identification of the "slope-breaks" mapped as end points along the radial profiles of Fig. 5.

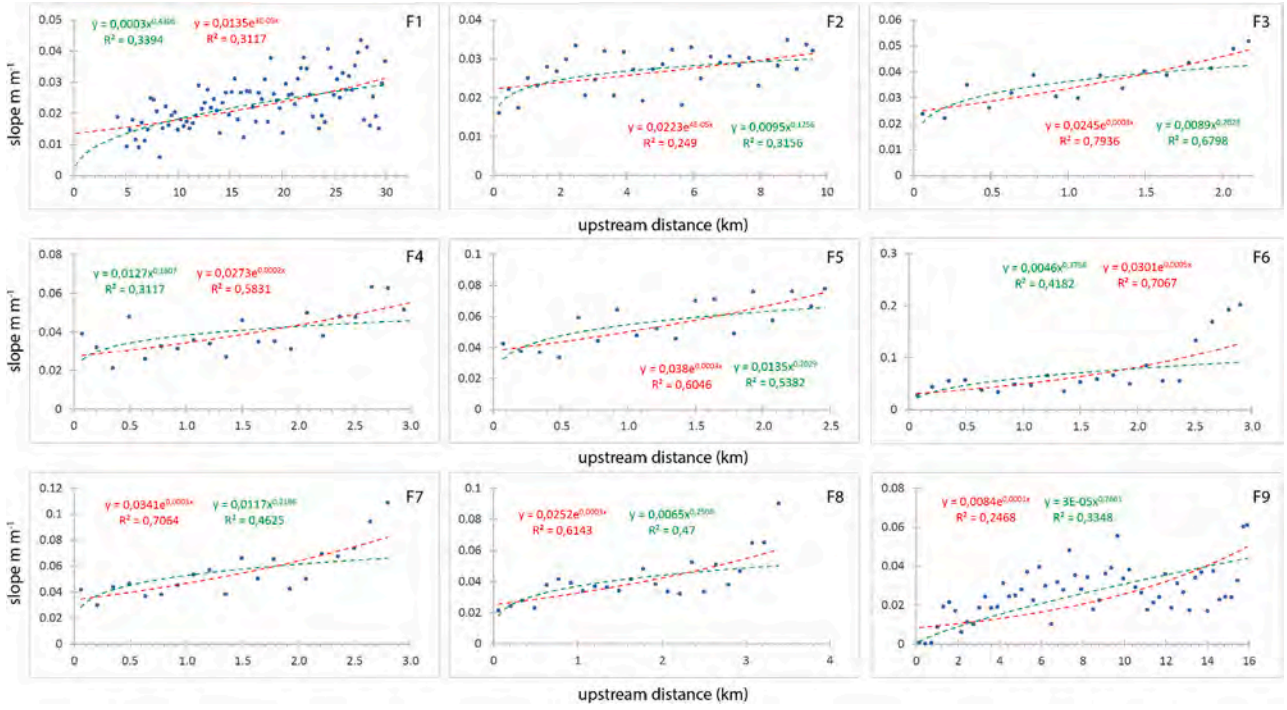

Fig. 13. The regression analysis of F1-F9. The red and green dotted line represent the exponential and the power law regression, respectively. The equations and R^2 coefficient are reported in each graph.

The identification of "slope-breaks" along each profile allows the remapping of F1-F9 fans as reported in Fig. 12.

4.4. Regression analysis on fan axis

The remapped fans F1-F9 were used to trace the fan axis as the median between the apex and the distal edge. Along each fan axis, the slope values were filtered using a moving average filter for improving the fitting of the regression analysis. Specifically, the moving average filter is computed using a sliding window of length 5 or 10 for the smallest (F3-F8) and larger fans (F1/F2/F9), respectively.

In Fig. 13 the largest alluvial fans F1, F2, and F9 are better interpolated by the power law regression despite the R^2 coefficient keeping low values of about 0.3. In contrast, the alluvial fans F3-F8 are better described by the exponential regression as also confirmed by the R^2 coefficient that increases up to 0.79 in F3. The slope along the fan axis of F1, F2, and F9 is quite low (0.05 m m^{-1}) reaching the maximum in the apex sector of F9 (0.06 m m^{-1}). The lowest difference between the power law R^2 coefficient and the exponential one in F1 (0.028) makes identification of the best linear fitting (power law or exponential) quite uncertain. Instead, the difference between R^2 coefficients in F2 and F9 is slightly greater (0.067 and 0.088, respectively); the power law regression seems to offer the best linear fitting.

Among the fans described through the exponential regression, F6, F7, and F8 clearly show a significant increase in the slope in the apex sector where the last points reach 0.1–0.2 m m^{-1}. F3, F4, and F5 present an apex sector less sloped with values around 0.05–0.08 m m^{-1}.

The mean slope of the "exponential fans" (i.e., F3-F8) are higher than the one observed in the "power fans" (i.e., F1/F2/F9) with values around 0.04 m m^{-1} up to 0.08 m m^{-1} like in F6, while F1, F2, and F9 have a quite low mean slope (0.02–0.03 m m^{-1}). As previously observed in the S-A analysis, in the regression analysis F1, F2, and F9 are different from F3-F8, thus potentially suggesting different depositional mechanisms.

4.5. Cluster analysis

The table available in the Supplementary materials 3 summarizes the main morphometric parameters and the mean annual precipitation of each feeding catchment, which is considered here for distinguishing the alluvial fans of the study area. Due to the relevant difference among the fans, we considered the normalized values according to the range scaling method.

We first compared the normalized values of fan and catchment areas (F_a and C_a), total channel length of the catchment (C_{cl}), fan axis length (F_l), fan mean slope (F_s), and catchment Melton Roughness (C_{mr}) (Fig. 14). The area of the feeding catchments (C_a) is directly related to the area of the corresponding alluvial fan (F_a) (Fig. 14a), as well as the total channel length of the feeding catchments (C_{cl}) is directly proportional to the corresponding alluvial fan area (F_a) (Fig. 14b). Conversely, the fan axis length (F_l) is inversely correlated to its mean slope (F_s) (Fig. 14c), as the fan mean slope (F_s) and the catchment Melton Roughness (C_{mr}) (Fig. 14d). The R^2 coefficients of the plots with direct proportion are quite higher: 0.96 and 0.94. The R^2 coefficient decreases to 0.42 in the F_l-F_s plot, while in the F_s-C_{mr} plot is 0.81. However, there is clustering of F3-F8 fans in each graph, whereas F1, F2, and F9 are rather distant from each other, except in Fig. 14d. Specifically, in the first two plots (Fig. 14a and b), the F3-F8 fans are characterized by smallest areas and shortest drainage networks in the feeding catchments; hence, they are proximal to the origin. Instead, F3-F8 fans are less grouped in the F_l-F_s plot because the normalized slopes along their fan axes vary between 0.333 and 1.00, while the normalized axis length is quite short (below 0.049). Similarly, F3-F8 fans are less grouped in the F_s-C_{mr} plot.

We next conducted *k-means* clustering analysis to explore the correlation between the morphometric characteristics of both fans and their respective catchments, as well as the clustering tendency between FFs and AFs. Fig. 15a shows the t-SNE cluster plot and the summary statistics of the two-cluster model whose accuracy is about 0.502. The cluster analysis distinguished two groups where cluster 1 is formed by F3-F8 fans, and cluster 2 is F1, F2, and F9.

In the plots of Fig. 14 F2, and F9 are between two end members (F1 on one hand, and F3-F8 on the other one). The same framework can be observed in the t-SNE cluster plot (Fig. 15a) where F2 and F9 are clustered together to F1 (cluster 2) despite them being quite proximal to cluster 1 (F3-F8). Once again, the main distinction is between the F1/F2/F9 group ("power fans"), and F3-F8 ("exponential fans"), as in the S-

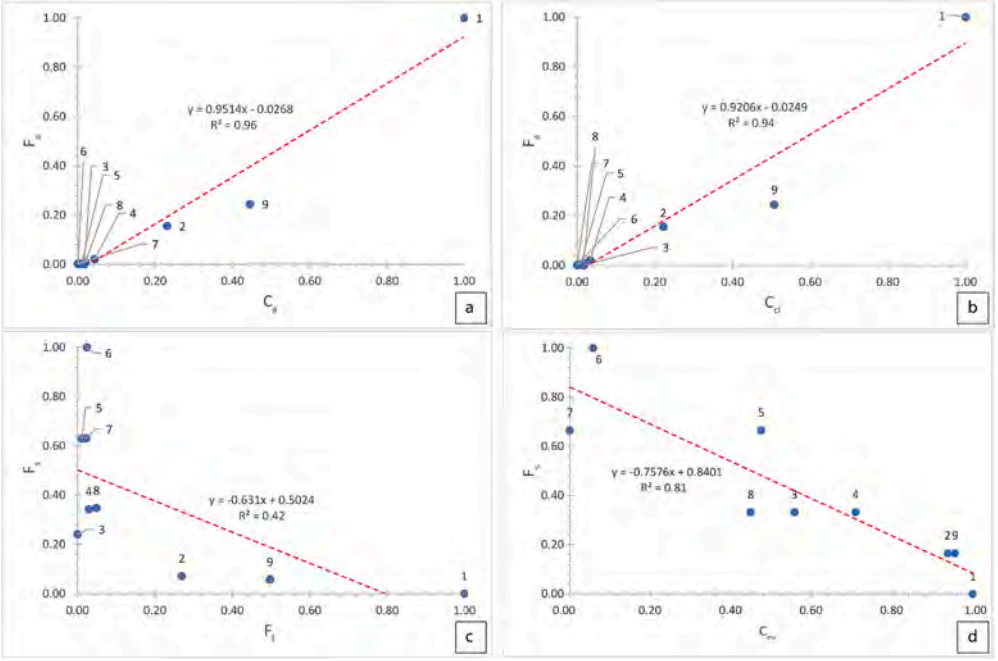

Fig. 14. Scatter plots of the normalized values of fan area vs catchment area (C_a vs F_a) (a), the channel length in the feeding catchments vs the area of the alluvial fan (C_{cl} vs F_a) (b), the length of the fan axis vs the mean slope (F_l vs F_s) (c), and the catchment roughness vs fan mean slope (C_{mr} vs F_s) (d).

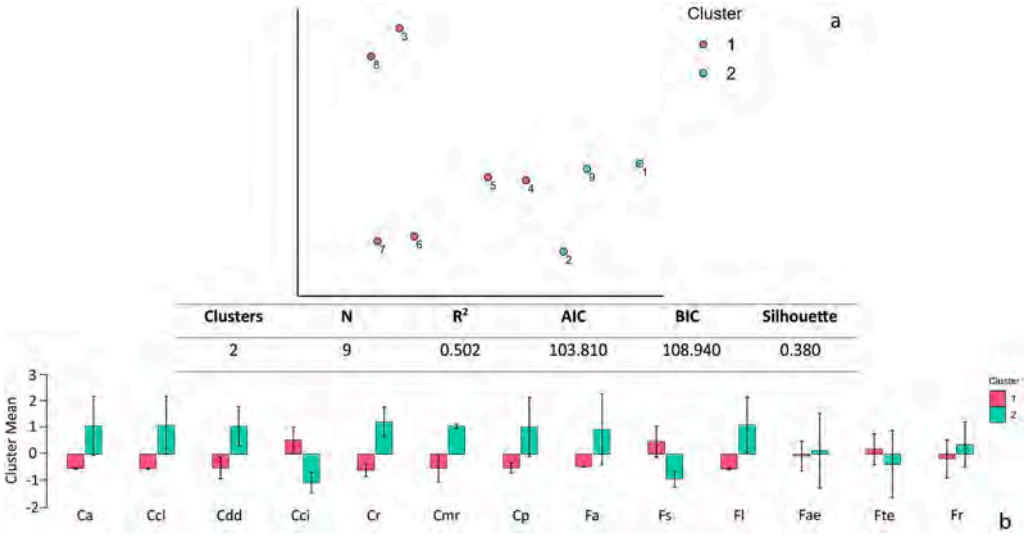

Fig. 15. The t-SNE cluster plot (a) and the cluster mean plot (b) obtained in JASP 0.16.4.0.

A analysis.

Observing the morphometric parameters of the feeding catchments (Supplementary materials 3), specifically the area and the channel length, F3-F8 are characterized by the smallest areas and the shortest drainage networks. On the other hand, F1/F2/F9 have the widest feeding catchments and the longest drainage networks, despite F2 being characterized by lower values than F1 and F9. After considering the morphometric parameters of the alluvial fans, the distinction between F3-F8 and F1/F2/F9 is less evident because only F1 seems discernible thanks to its widest area (358.81 km^2), longest fan axis (29.79 km), and lowest mean slope (0.02 m m^{-1}).

In the cluster mean plot (Fig. 15b) the difference between cluster 1

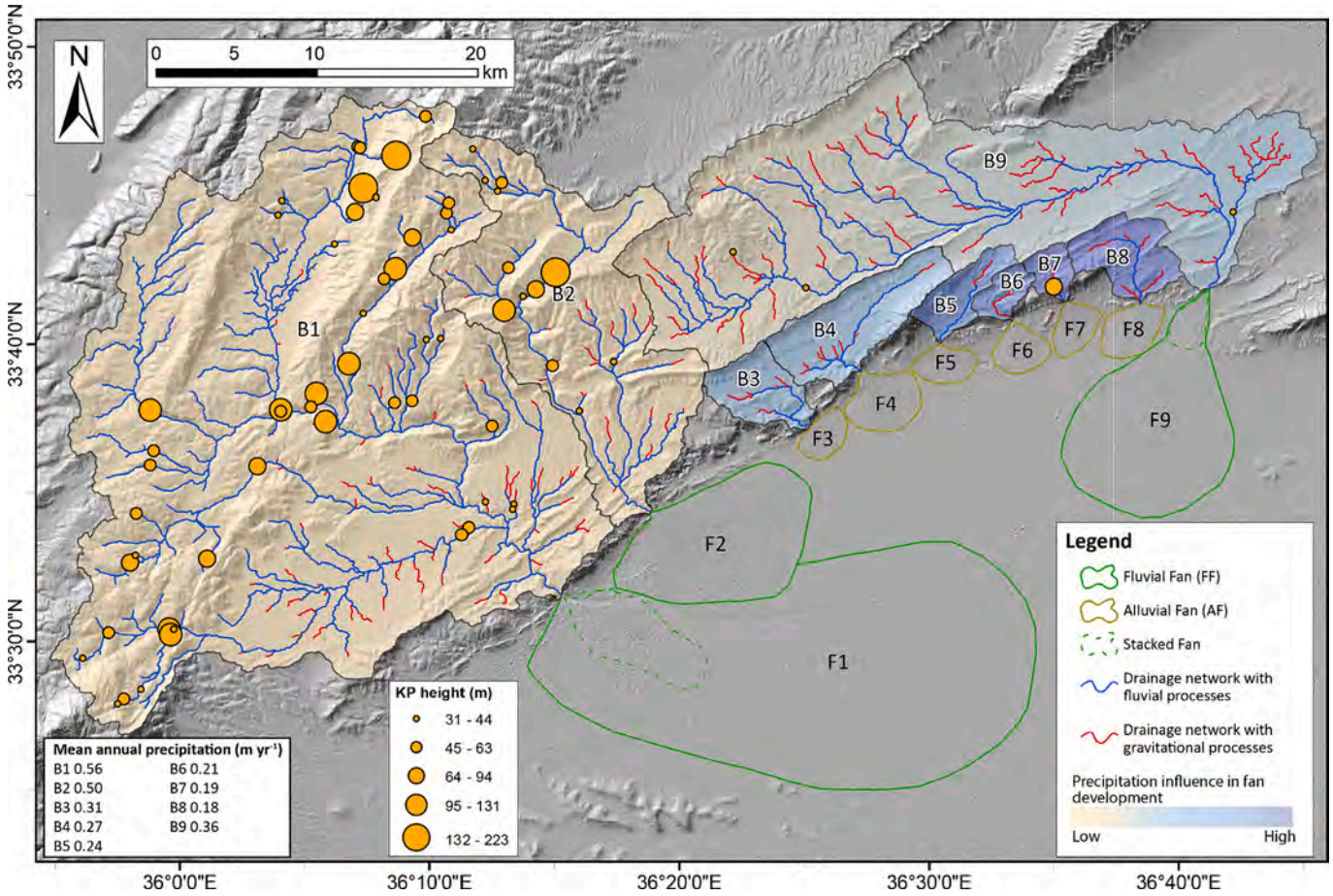

Fig. 16. The final sketch with the main outputs: the remapping of the fans and their distinction according the prevailing construction process (FFs and AFs), thus highlighting the frequency of the stacked fans. The feeding catchments are distinguished considering the precipitation contribution in the delineation of the prevailing construction process of the fans. The drainage networks are discerned according to the outputs derived from the S-A analysis.

and cluster 2 is quite obvious in each category except when we consider the F_a, F_{ae}, F_{te}, and F_r. The cluster means of C_a, C_{cl}, C_{dd}, C_r, C_{mr}, and C_p—as well as F_a, F_l, F_{ae}, and F_r—vary approximately between 0 and 1 for cluster 2. The mean is below 0 in cluster 1. Conversely, the cluster means of F_g, C_{ci}, and F_{te} are marked by positive values for cluster 1 and negative ones for cluster 2.

The cluster mean plot can help infer the most suitable parameters for discerning the two clusters. In fact, the feeding catchment parameters fully distinguished the two clusters whose quartiles are well separated. Rather, some fan parameters (e.g., F_a, F_{ae}, F_{te}, F_r) seem to be less suitable for discerning the two clusters, while the quartiles of F_s and F_l are nicely separated (Fig. 15b), thus clearly discerning the two clusters.

5. Discussion

5.1. Coalescing alluvial fans geomorphological mapping

Nine alluvial fans (named F1-F9) were confirmed along the southern margin of the ALM close to the Damascus intermontane basin. Their geomorphological characterization and mapping have been improved (Fig. 16). The construction of radial profiles and the extraction of contour lines mark the end points and thus delineating the piedmont fans. They also recognize the adjacent fans that coalescence as in F1 and F2. The latter has a convex-up profile along the radial profile p7 in Fig. 10, thus suggesting the superposition of F2 deposits above F1.

Both radial profiles and contour lines (Supplementary materials 2) show clear differences between the delineated and remapped fans as the ones provided by the Geomorphological Map of Syria at 1:1,000,000 scale (1963) as shown in Fig. 12. Specifically, several fans present shifted apex points and different plan shapes, mainly due to the difference in the scale of investigation (1,1,000,000 vs 1:200,000 of the present work). Moreover, the radial profiles of the largest fans F1 and F9 allow us to recognize the plausible occurrence of a stacked fan structure. Indeed, their profiles along the apex sectors have the steepest slopes with values greater than the first standard deviation (specifically, profiles p4-p7 for F1 as well as p2-p4 for F9 in Supplementary materials 1). The middle sectors are characterized by slope values proximal to the first standard deviation or between the mean and the standard deviation. Finally, the area beyond the end points is characterized by slope values lower than the mean. The identification of these three different sectors only above the largest fans F1 and F9 suggests the development of smallest fans exclusively in their apex sectors as typically recognisable in the "stacked" fans (Fig. 16).

5.2. Fan construction processes

The difference in the prevailing construction process among the piedmont fans of the study area was first suggested by their remapping. Specifically, the smallest fans (F3-F8) have confined catchments and a short fan axis, while the largest fans (F1, F2, and F9) have wide catchments and long fan axis. As reported by Ventra and Clarke (2018), Harvey (2018), and Moscariello (2018), these morphometric characteristics are the most indicative for discerning between AF and FF.

The distinction between F3-F8 and F1/F2/F9 found in each step of the workflow may be helpful for obviating the absence of field investigation, thus validating the complete remote-desk approach adopted here.

We first considered the S-A functions to connect this cluster tendency with the prevailing construction process. Precisely, the feeding catchments of the largest fans F1/F2/F9 show a well-developed fluvial domain that is less pronounced in B3-B8 (not weighted data). Indeed, the occurrence of fluvial processes can be easily seen in Fig. 6c where there is a greater distance between the thresholds and maximum values, and thus a greater development of the fluvial domain.

Considering the rainfall's influence, it is evident that the eastward aridification may play a relevant role, especially in the smallest catchments (B3-B8). The plots in Fig. 6b suggest the eastward increasing distance between not-weighted vs weighted data that we can associate with the role of the different climatic conditions in the drainage network development: a greater distance between weighted and not-weighted data implies a greater influence of precipitation. Specifically, we note the role of precipitation in B6 where the fluvial domain is not developed at all. Therefore, the absence of a marked fluvial domain in the smallest catchments (B3-B8), in addition to a seasonal distribution of rainfall, suggests that the occurrence of extreme events like debris flows played a significant role in the fan development (Fig. 16). Moreover, we suppose that the influence of precipitation in B9 may be intermediate, given the longitudinal extent of the basin with the western sector less influenced than the eastern one (Fig. 16).

The distinction of construction process seems to be also evident in the regression analysis applied to the upslope profiles. F3-F8 have been described as "exponential fans" since the increasing slope values, especially in the apex sectors, easily defines a straightforward concave-up profile especially in F6-F8. Therefore, the selection of the most suitable regression has been easier considering the highest values of R^2 (>0.6). In this manner, a steeper profile (up to 0.08 m m^{-1}) and shortest axis (few km), typical of AFs (Bull, 1977; Blair and McPherson, 2009; Ventra and Clarke, 2018; Harvey, 2018; Moscariello, 2018), allow us to confirm the preliminary distinction in the construction process between F3-F8 and F1/F2/F9. The latter could be potentially defined as "power fans" since the constant increase of the slope values apex-ward is describable through a power law regression that is typically associated with FFs (Williams et al., 2006). However, the quite low value of R^2 (below 0.34) is weak for selecting the most suitable regression, thus leaving the definition of "power fans" rather unsure.

The plots of Fig. 14 show that F1/F2/F9 have long axes of several tens of kilometres (10–30 km) and rather low slopes (below 0.03 m m^{-1}). These two features are typically seen in FFs as reported elsewhere (Bull, 1977; Kostaschuk et al., 1986; Blair and McPherson, 2009; Ventra and Clarke, 2018; Harvey, 2018; Moscariello, 2018). Therefore, we conclude that the regression analysis is more suitable for recognizing AFs than FFs, where the identification of the prevailing construction process seems to be clearer. Conversely, the poor feasibility of the regression analysis over the largest fans may be due to a more complex development mechanism and morphodynamics (e.g., alternation of fluvial and gravitational processes, occasional occurrence of hyperconcentrated flows, etc.).

A further distinction in the construction process has been obtained through the computation of the cluster analysis. Several catchment and fan parameters have been considered for defining the morphometric correlation between catchments and fans as well as for discovering the cluster tendency of the mapped landforms. The C_a vs F_a and C_{cl} vs F_a plots (Fig. 14) perfectly describe the typical linear proportion (R^2 up to 0.96): there is a wider feeding catchment, a longer drainage network, and thus a higher fan area. Likewise, there is a well-known correlation between F_l and F_s: they are inversely proportional despite the coefficient of determination being low (0.42). Conversely, F_s and C_{mr} are inversely related in the present study, contrasting some previous works (e.g., Kostaschuk et al., 1986; Crosta and Frattini, 2004; Karymbalis et al., 2016). F_s and C_{mr} are relevant morphometric parameters for defining the fan energy in the construction process: AFs are characterized by higher C_{mr} and F_s than FFs (Karymbalis et al., 2016). In the present study, F3-F8 are characterized by highest slopes ($F_s > 0.33$) and low catchment roughness ($C_{mr} > 0.7$); while F1/F2/F9 present lowest slopes ($F_s < 0.16$) and high catchment roughness ($C_{mr} > 0.9$). We can explain this controversial tendency considering the catchment size (several hundreds vs few tens of km^2). B1/B2/B9 are the widest basins characterized by various landscapes (i.e., medium - height mountains with flattened divides, steep slopes, low mountains with small and low ridges, and low mountains with coniform and cuesta-hilly relief), that may result in the highest relief. Conversely, B3-B8 are the smallest catchments with a quite homogeneous landscape (mountains of medium height with

narrow divides and longitudinal valleys), and their relief may be lower.

In each plot of Fig. 14, we see again the separation of F1/F2/F9 from F3-F8 as confirmed by the cluster analysis. Indeed, the optimized *k-means* clustering according to BIC value was perfectly recognized in the two groups, where most of the selected parameters straightforwardly distinguish cluster 1 (F3-F8) from cluster 2 (F1/F2/F9). The maximum distinction between the two clusters can be observed in almost all parameters, especially for the catchment ones (as already observed by Crosta and Frattini (2004)), while F_a, F_{ae}, F_{te}, and F_r are less suitable. Hence, we can infer that the parameters of the feeding catchments seem to be the most suitable variables for discriminating the prevailing construction process, while the morphometric fan parameters like slope and length are more significant when compared to the catchment parameters.

The role of tectonics in fan development was also considered including the literature about the Damascus reverse fault. Abou Romieh et al. (2009) have estimated a significant slip rate that was successively confirmed by the inferred Late Pleistocene fluvial terraces of Barada River (Abou Romieh et al., 2012). Moreover, the Damascus reverse faults developed a throw of about 2500 m and activated about 0.9 Ma with an estimated vertical slip rate of about 2.8 mm yr-1 (Abou Romieh et al., 2012). However, the low slip rate geodetically measured along the Palmyrides ($\sim 1.5 \pm 1.0$ mm yr-1 from Alchalbi et al., 2010), as well as the quasi-total absence of significant earthquakes in the study area (Fig. 2), may be explained by the crustal shortening within the PFB (Abou Romieh et al., 2012).

Moreover, from longitudinal river profiles, it was possible to observe that the non-lithological knickpoints are concentrated in the B1 and B2 basins, where the fault is likely to have had its maximum slip, effectively generating a greater accommodation space. The knickpoints in the B9 basin, on the other hand, are probably due to fluvial captures. Indeed, we can observe the straightforward westward development of the basin (lowest C_{ci}), in addition to the occurrence of the rectangular drainage pattern. Therefore, tectonic impacts on fan development would have been greater in B1 and B2, creating the maximum accommodation space. Therefore, tectonic impacts on fan development would have been greater in B1 and B2.

The absence of the stacked structures along the radial profiles of F2 would also seem to suggest that the tectonic input may play a minor role in fan development in the study area. The occurrence of stacked structures only in F1 and F9 may be correlated with human activity. Indeed, the river management along the Barada River, as well as the mining activities in B1 and B9 may have modified the base level, thus favouring the stacked framework.

Heterogeneous lithologies undoubtedly play a key role in the development of the piedmont alluvial fans (Bull, 1968; Harvey et al., 2005; Blair and McPherson, 2009). However, the lithological map reported in Fig. 2a shows a very homogeneous distribution of lithologies in the basins with the highest variability in the largest basins (B1, B2, and B9). Moreover, we can infer that the erodibility may be quite homogeneous among basins considering the prevailing outcrop of limestones and limestones/marl alternations.

Despite the low resolution of the SRTMv3 DEM, the proposed workflow has successfully unravelled the distinction between FFs and AFs along the southern margin of the ALM. The insights are suitable for the regional investigation of several piedmont fans as in the study area where the construction processes have not yet been defined. However, geomorphological field work is essential for confirming these results as well as for cross-checking what is preliminary identified by remote analysis. For example, sedimentological analysis is essential for describing the active/abandoned zones (e.g., fan head, trunk channel, distributary channels) and for characterizing sediment flows and for inferring the lithological setting of the feeding catchment.

6. Conclusions

The southern margin of the ALM preserves nine alluvial fans (F1-F9) that longitudinally occupy the piedmont sector for about 50 km. The size and the characteristics of the physical landscape of the study area strongly favoured a remote methodological approach. The remotely-desk investigation of the area offered geomorphological characterization and classification via the construction process of the alluvial fans previously mapped in the Geomorphological Map of Syria at 1:1,000,000 scale. The proposed methodological approach using the 30 m SRTMv3 DEM is suitable for the regional investigations of alluvial fans in semi-arid zones.

The main outcomes can be summarised as follows:

1. All alluvial fans previously reported in a rough way on an existing geological map have been remapped, thus delimiting the coalescent fans through the radial profiles and the extracted contour lines.
2. The S-A analysis of the feeding catchments is suitable for defining the role of the spatial rainfall gradient, as well as for delineating the initiation of the fluvial domain.
3. Regression analysis over the upslope profiles is potentially useful for a preliminary distinction of the AFs where the exponential regression can be applied.
4. Cluster analysis that considered parameters of both feeding catchments and fans is the critical step for straightforwardly discerning the prevailing construction process, especially considering the catchment parameters as well as the fan length and slope.
5. The FFs (F1/F2/F9) are characterized by widest areas, longest axis, and lowest slopes; moreover, F1 and F9 can be defined as stacked fans that are typical of active mountain fronts (e.g., Damascus reverse fault). On the other hand, the AFs (F3-F8) have smallest areas, shortest axis, and highest slopes.
6. The rainfall influence increases eastward favouring the fluvial-dominated processes in the wider catchments as well as run-off events in smaller catchments.
7. The role of tectonics is relevant in the westernmost sector (B1-B2), where the slip of the Damascus fault may be maximum and may develop the greater accommodation space.

Finally, wide and inaccessible areas can be potentially investigated using the approach proposed here especially where arid and semi-arid climate conditions prevail as well as where socio-political issues may prevent effective field work.

Supplementary data to this article can be found online at https://doi.org/10.1016/j.geomorph.2024.109148.

CRediT authorship contribution statement

Giulia Iacobucci: Writing – review & editing, Writing – original draft, Visualization, Software, Methodology, Investigation, Formal analysis, Conceptualization. **Michele Delchiaro:** Writing – review & editing, Writing – original draft, Visualization, Software, Methodology, Formal analysis. **Francesco Troiani:** Writing – review & editing, Supervision, Project administration, Methodology, Conceptualization. **Davide Nadali:** Writing – review & editing, Project administration, Funding acquisition.

Declaration of competing interest

The authors declare that they have no known competing financial interests or personal relationships that could have appeared to influence the work reported in this paper.

Data availability

Data will be made available on request.

Acknowledgments

We thank the executive Guest Editor Dr. Frederic Liebault and Guest Editor Dr. Vittoria Scorpio. We also thank Dr. Martin Stokes, Dr. Gianluca Norini, and three other anonymous reviewers for their critical comments on the manuscript. We also like to thank LG for all the entertainment. This work was supported by the grant from the Italian Ministry of Education, University and Research (MIUR) to Prof. Davide Nadali "Fluid Crescent. Water and Life in the Societies of the Ancient Near East" (PRIN 2017NMK5FE_001).

References

Abdul-Wahed, M.K., 2022. New insights into the seismic activity of Damascus Fault (Syria): a quantitative analysis. Geofis. Int. 61 (2), 88–99. https://doi.org/10.22201/igeof.00167169p.2022.61.2.2054.

Abou Romieh, M., Westaway, R., Daoud, M., Radwan, Y., Yassminh, R., Khalil, A., al-Ashkar, A., Loughlin, S., Arrell, K., Bridgland, D., 2009. Active crustal shortening in NE Syria revealed by deformed terraces of the River Euphrates. Terra Nova 27, 427–437. https://doi.org/10.1111/j.1365-3121.2009.00896.x.

Abou Romieh, M., Westaway, R., Daoud, M., Bridgland, D.R., 2012. First indications of high slip rates on active reverse faults NW of Damascus, Syria, from observations of deformed Quaternary sediments: implications for the partitioning of crustal deformation in the Middle Eastern region. Tectonophysics 538–540, 86–104. https://doi.org/10.1016/j.tecto.2012.03.008.

Adams, B.A., Whipple, K.X., Forte, A.M., Heimsath, A.M., Hodges, K.V., 2020. Climate controls on erosion in tectonically active landscapes. Science. Advances 6 (42), eaaz3166. https://doi.org/10.1126/sciadv.aaz3166.

Alchalbi, A., Daoud, M., Gomez, F., McClusky, S., Reilinger, R., Romeyeh, M.A., Alsouod, A., Yassminh, R., Ballani, B., Darawcheh, R., Sbeinati, R., Radwan, Y., Masri, R.A., Bayerly, M., Ghazzi, R.A., Barazangi, M., 2010. Crustal deformation in northwestern Arabia from GPS measurements in Syria: Slow slip rate along the northern Dead Sea Fault. Geophys. J. Int. 180, 125–135. https://doi.org/10.1111/j.1365-246X.2009.04431.x.

Baba, A., Karem, R.A., Yazdani, H., 2021. Groundwater resources and quality in Syria. Groundw. Sustain. Dev. 14, 100617 https://doi.org/10.1016/j.gsd.2021.100617.

Babič, M., Petrovič, D., Sodnik, J., Soldo, B., Komac, M., Chernieva, O., Calì, M., 2021. Modeling and Classification of alluvial fans with DEMs and machine learning methods: a case study of Slovenian torrential fans. Remote Sens. 13 (9), 1711. https://doi.org/10.3390/rs13091711.

Barazangi, M., Seber, D., Chaimov, T., Best, J., Sawaf, T., 1993. Tectonic evolution of the northern Arabian plate in western Syria. In: Boschi, E., Mantovani, E., Morelli, A. (Eds.), Recent Evolution and Seismicity of the Mediterranean Region. Kluwer Academic Publishers, pp. 117–140. https://doi.org/10.1007/978-94-011-2016-6_5.

Benito, G., 2013. 13.15 hazardous processes: flooding. In: Shroder, J.F. (Ed.), Treatise on Geomorphology, vol. 13. Academic Press, pp. 243–261. https://doi.org/10.1016/B978-0-12-374739-6.00363-8.

Blair, T.C., McPherson, J.G., 2009. Processes and forms of alluvial fans. In: Parsons, A.J., Abrahams, A.D. (Eds.), Geomorphology of Desert Environments. Springer, Dordrecht, pp. 413–468. https://doi.org/10.1007/978-1-4020-5719-9_14.

Boulton, S.J., Stokes, M., 2018. Which DEM is best for analyzing fluvial landscape development in mountainous terrains? Geomorphology 310, 168–187. https://doi.org/10.1016/j.geomorph.2018.03.002.

Brew, G., Barazangi, M., Al-Maleh, A.K., Sawaf, T., 2001. Tectonic and geologic evolution of Syria. GeoArabia 6 (4), 573–616. https://doi.org/10.2113/geoarabia0604573a.

Bull, W.B., 1968. Alluvial fans. J. Geol. Educ. 16 (3), 101–106. https://doi.org/10.5408/0022-1368-XVI.3.101.

Bull, W.B., 1977. The alluvial-fan environment. Progress in Physical Geography: Earth and Environment 1 (2), 222–270. https://doi.org/10.1177/030913337700100202.

Chelli, A., Bordoni, M., Cappadoni, C., Pepe, G., Rotigliano, E., Smith, M., 2021. Geomorphological tools for mapping natural hazards. J. Maps 17 (3), 1–4. https://doi.org/10.1080/17445647.2021.1920794.

Cracknell, M.J., Reading, A.M., 2014. Geological mapping using remote sensing data: a comparison of five machine learning algorithms, their response to variations in the spatial distribution of training data and the use of explicit spatial information. Comput. Geosci. 63, 22–33. https://doi.org/10.1016/j.cageo.2013.10.008.

Crosta, G.B., Frattini, P., 2004. Controls on modern alluvial fan processes in the central Alps, northern Italy. Earth Surface Processes and Landforms. The Journal of the British Geomorphological Research Group 29 (3), 267–293.

Crouvi, O., Ben-Dor, E., Beyth, M., Avigad, D., Amit, R., 2006. Quantitative mapping of arid alluvial fan surfaces using field spectrometer and hyperspectral remote sensing. Remote Sens. Environ. 104 (1), 103–117. https://doi.org/10.1016/j.rse.2006.05.004.

Delchiaro, M., Fioramonti, V., Della Seta, M., Cavinato, G.P., Mattei, M., 2021. Fluvial inverse modeling for inferring the timing of Quaternary uplift in the Simbruini range (Central Apennines, Italy). Trans. GIS 25 (5), 2455–2480. https://doi.org/10.1111/tgis.12833.

Delchiaro, M., Iacobucci, G., Troiani, F., Della Seta, M., Ballato, P., Aldega, L., 2022. Morphoevolution of the Seymareh landslide-dam lake system (Zagros Mountains, Iran): implications for Holocene climate and environmental changes. Geomorphology 413, 108367. https://doi.org/10.1016/j.geomorph.2022.108367.

Delchiaro, M., Della Seta M., Martino, S., Nozaem, R., Moumeni, M., 2023. Tectonic deformation and landscape evolution inducing mass rock creep driven landslides: the Loumar case-study (Zagros Fold and Thrust Belt, Iran). Tectonophysics 846, 229655. https://doi.org/10.1016/j.tecto.2022.229655.

El Fels, A.E.A., El Ghorfi, M., 2022. Using remote sensing data for geological mapping in semi-arid environment: a machine learning approach. Earth Sci. Inf. 15, 485–496. https://doi.org/10.1007/s12145-021-00744-w.

Elkhrachy, I., 2018. Vertical accuracy assessment for SRTM and ASTER Digital Elevation Models: a case study of Najran city. Saudi Arabia. Ain Shams Engineering Journal 9 (4), 1807–1817. https://doi.org/10.1016/j.asej.2017.01.007.

Expósito, I., Jiménez-Bonilla, A., Delchiaro, M., Yanes, J.L., Balanyá, J.C., Moral-Martos, F., Della Seta, M., 2022. Geomorphic signature of segmented relief rejuvenation in the Sierra Morena, Betic forebulge. Spain. Earth Surface Dynamics 10 (5), 1017–1039. https://doi.org/10.5194/esurf-10-1017-2022.

Fick, S.E., Hijmans, R.J., 2017. WorldClim 2: new 1-km spatial resolution climate surfaces for global land areas. Int. J. Climatol. 37 (12), 4302–4315. https://doi.org/10.1002/joc.5086.

Field, J.J., Pearthree, P.A., 1997. Geomorphologic flood-hazard assessment of alluvial fans and piedmonts. J. Geosci. Educ. 45 (1), 27–37. https://doi.org/10.5408/1089-9995-45.1.27.

Harvey, A.M., 2005. Differential effects of base-level, tectonic setting and climatic change on Quaternary alluvial fans in the northern Great Basin, Nevada, USA. Geol. Soc. Lond. Spec. Publ. 251 (1), 117–131.

Harvey, A., 2018. Alluvial fans. In: Reference Module in Earth Systems and Environmental Sciences. https://doi.org/10.1016/B978-0-12-409548-9.11066-8.

Harvey, A., Mather, A., Stokes, M., 2005. Alluvial fans: geomorphology, sedimentology, dynamics – introduction. A review of alluvial-fan research. In: Harvey, A., Mather, A., Stokes, M. (Eds.), Alluvial Fans: Geomorphology, Sedimentology, Dynamics, Geological Society, London, Special Publications, vol. 251, pp. 1–7. https://doi.org/10.1144/GSL.SP.2005.251.01.01 (2005).

Iacobucci, G., Troiani, F., Milli, S., Mazzanti, P., Piacentini, D., Zocchi, M., Nadali, D., 2020. Combining satellite multispectral imagery and topographic data for the detection and mapping of fluvial avulsion processes in lowland areas. Remote Sens. 12 (14), 2243.

Iacobucci, G., Piacentini, D., Troiani, F., 2022a. Enhancing the identification and mapping of fluvial terraces combining geomorphological field survey with land-surface quantitative analysis. Geosciences 12 (11), 425. https://doi.org/10.3390/geosciences12110425.

Iacobucci, G., Troiani, F., Milli, S., Nadali, D., 2022b. Geomorphology of the lower Mesopotamian plain at Tell Zurghul archaeological site. J. Maps. https://doi.org/10.1080/17445647.2022.2112772.

JASP Team, 2023. JASP version 0.17 Computer Software. https://jasp-stats.org/. (Accessed 31 January 2023).

Karymbalis, E., Ferentinou, M., Giles, P.T., 2016. Use of morphometric variables and self-organizing maps to identify clusters of alluvial fans and catchments in the north Peloponnese, Greece. Geol. Soc. Lond. Spec. Publ. 440 (1), 45–64. https://doi.org/10.1144/sp440.7.

Karymbalis, E., Ferentinou, M., Fubelli, G., Giles, P., Tsanakas, K., Valkanou, K., Batzakis, D.V., Karalis, S., 2022. Classification of Trichonis Lake graben (Western Greece) alluvial fans and catchments using geomorphometry and artificial intelligence. Annals of Geomorphology 63 (2–3), 295–312. https://doi.org/10.1127/zfg/2022/0748.

Kattan, Z., 2006. Characterization of surface water and groundwater in the Damascus Ghotta basin: hydrochemical and environmental isotopes approaches. Environ. Geol. 51 (2), 173–201. https://doi.org/10.1007/s00254-006-0316-z.

Knight, J., Mitchell, W.A., Rose, J., 2011. Chapter six - geomorphological field mapping. In: Smith, M.J., Paron, P., Griffiths, J.S. (Eds.), Developments in Earth Surface Processes. Elsevier, pp. 151–187. https://doi.org/10.1016/B978-0-444-53446-0.00006-9.

Kostaschuk, R.A., Macdonald, G.M., Putnam, P.E., 1986. Depositional process and alluvial fan-drainage basin morphometric relationships near banff, Alberta. Canada. Earth Surface Processes and Landforms 11 (5), 471–484. https://doi.org/10.1002/esp.3290110502.

Macklin, M.G.; Lewin, J. 2015. The rivers of civilization. Quat. Sci. Rev., 114, 228–244. https://doi.org/https://doi.org/10.1016/j.quascirev.2015.02.004.

McFadden, L.D., Ritter, J.B., Wells, S.G., 1989. Use of multiparameter relative-age methods for age estimation and correlation of alluvial fan surfaces on a desert piedmont, eastern Mojave Desert. California. Quaternary Research 32 (3), 276–290. https://doi.org/10.1016/0033-5894(89)90094-X.

Melton, M.A., 1965. The geomorphic and paleoclimatic significance of alluvial deposits in southern Arizona. J. Geol. 73 (1), 1–38.

Mokarram, M., Seif, A., Sathyamoorthy, D., 2014. Use of morphometric analysis and self-organizing maps for alluvial fan classification: case study on Ostorankooh altitudes, Iran. In: IOP Conference Series: Earth and Environmental Science, 20, 7th IGRSM International Remote Sensing & GIS Conference and Exhibition 22–23 April 2014, Kuala Lumpur, Malaysia. https://doi.org/10.1088/1755-1315/20/1/012003.

Mokarram, M., Pourghasemi, H.R., Tiefenbacher, J.P., 2022. Identification of morphometric features of alluvial fan and basins in predicting the erosion levels using ANN. Environ. Earth Sci. 81 (3), 95. https://doi.org/10.1007/s12665-022-10219-w.

Moscariello, A., 2018. Alluvial fans and fluvial fans at the margins of continental sedimentary basins: geomorphic and sedimentological distinction for geo-energy exploration and development. In: Ventra, D., Clarke, L. (Eds.), Geology and Geomorphology of Alluvial and Fluvial Fans: Terrestrial and Planetary Perspectives, Geological Society, London, Special Publications, vol. 440(1), pp. 45–64. https://doi.org/10.1144/SP440.11.

Moumeni, M., Delchiaro, M., Della Seta, M., Nozaem, R., Ballato, P., Leonard, J.S., Rouhi, J., 2024. Interplay between tectonics and surface processes in the evolution of mountain ranges: insights from landscape dynamics, uplift, and active deformation of Talesh Mountains (NW Iranian Plateau margin). Geomorphology 448, 109029. https://doi.org/10.1016/j.geomorph.2023.109029.

Mukul, M., Srivastava, V., Jade, S., Mukul, M., 2017. Uncertainties in the Shuttle Radar Topography Mission (SRTM) Heights: insights from the Indian Himalaya and Peninsula. Sci. Rep. 7, 41672 https://doi.org/10.1038/srep41672.

Norini, G., Zuluaga, M.C., Ortiz, I.J., Aquino, D.T., Lagmay, A.M.F., 2016. Delineation of alluvial fans from Digital Elevation Models with a GIS algorithm for the geomorphological mapping of the Earth and Mars. Geomorphology 273, 134–149. https://doi.org/10.1016/j.geomorph.2016.08.010.

Özpolat, E., Yıldırım, C., Görüm, T., Gosse, J.C., Sahiner, E., Sarikaya, M.A., Owen, L.A., 2022. Three-dimensional control of alluvial fans by rock uplift in an extensional regime: Aydın Range, Aegean extensional province. Sci. Rep. 12, 15306 (2022). https://doi.org/10.1038/s41598-022-19795-0.

Piacentini, D., Troiani, F., Torre, D., Menichetti, M., 2021. Land-surface quantitative analysis to investigate the spatial distribution of gravitational landforms along rocky coasts. Remote Sens. 13 (24), 5012. https://doi.org/10.3390/rs13245012.

Pirrotta, C., Parrino, N., Pepe, F., Tansi, C., Monaco, C., 2022. Geomorphological and morphometric analyses of the catanzaro trough (Central Calabrian Arc, Southern Italy): Seismotectonic implications. Geosciences 12 (9), 324. https://doi.org/10.3390/geosciences12090324.

Radebaugh, J., Ventra, D., Lorenz, R.D., Farr, T., Kirk, R., Hayes, A., Malaska, M.J., Birch, S., Yung-Chun, Liu Z., Lunine, J., Barnes, J., Le Gall, A., Lopes, R., Stofan, E., Wall, S., Paillou, P., 2018. Alluvial and fluvial fans on Saturn's moon Titan reveal processes, materials and regional geology. Geol. Soc. Lond. Spec. Publ. 440 (1), 281. https://doi.org/10.1144/SP440.6.

Santangelo, N., Daunis-i-Estadella, J., Di Crescenzo, G., Di Donato, V., Faillace, P.I., Martín-Fernández, J.A., Scorpio, V., 2012. Topographic predictors of susceptibility to alluvial fan flooding, Southern Apennines. Earth Surf. Process. Landf. 37 (8), 803–817. https://doi.org/10.1002/esp.3197.

Schwanghart, W., Scherler, D., 2014. TopoToolbox 2–MATLAB-based software for topographic analysis and modeling in Earth surface sciences. Earth Surf. Dyn. 2 (1), 1–7. https://doi.org/10.5194/esurf-2-1-2014.

Stock, J.D., Schmidt, K.M., Miller, D.M., 2008. Controls on alluvial fan long-profiles. GSA Bull. 120 (5–6), 619–640. https://doi.org/10.1130/B26208.1.

Stolle, A., Schwanghart, W., Andermann, C., Bernhardt, A., Fort, M., Jansen, J.D., Whitmann, H., Merchel, S., Rugel, G., Adhikari, B.R., Korup, O., 2019. Protracted river response to medieval earthquakes. Earth Surf. Process. Landf. 44 (1), 331–341.

Uuema, E., Ahi, S., Montibeller, B., Muru, M., Kmoch, A., 2020. Vertical accuracy of freely available global digital elevation models (ASTER, AW3D30, MERIT, TanDEM-X, SRTM, and NASADEM). Remote Sens. 12, 3482. https://doi.org/10.3390/rs12213482.

V\O Technoexport, 1963. Geomorphological map of Syria. https://esdac.jrc.ec.europa.eu/content/geomorphological-map-syria. (Accessed 31 January 2023).

V\O Technoexport, 1964. Geological map of Syria. https://esdac.jrc.ec.europa.eu/content/geological-map-syria. (Accessed 31 January 2023).

Ventra, D., Clarke, L., 2018. Geology and geomorphology of alluvial and fluvial fans: terrestrial and planetary perspectives. Geol. Soc. Lond. Spec. Publ. 440, 1–21. https://doi.org/10.1144/SP440.16.

Vergari, F., Troiani, F., Faulkner, H., Del Monte, M., Della Seta, M., Ciccacci, S., Fredi, P., 2018. The use of the slope–area function to analyse process domains in complex badland landscapes. Earth Surf. Process. Landf. https://doi.org/10.1002/esp.4496.

Verstappen, H.T., 2011. Chapter two - old and new trends in geomorphological and landform mapping. In: Smith, M.J., Paron, P., Griffiths, J.S. (Eds.), Developments in Earth Surface Processes. Elsevier, pp. 13–38. https://doi.org/10.1016/B978-0-444-53446-0.00002-1.

Walstra, J., Heyvaert, V.M.A., Verkinderen, P., 2010. Assessing human impact on alluvial fan development: a multidisciplinary case-study from Lower Khuzestan (SW Iran). Geodin. Acta 23 (5–6), 267–285. https://doi.org/10.3166/ga.23.267-285.

Weiss, D.J., Walsh, S.J., 2009. Remote sensing of mountain environments. Geogr. Compass 3 (1), 1–21. https://doi.org/10.1111/j.1749-8198.2008.00200.x.

Williams, R.M.E., Zimbelman, J.R., Johnston, A.K., 2006. Aspects of alluvial fan shape indicative of formation process: a case study in southwestern California with application to Mojave Crater fans on Mars. Geophys. Res. Lett. 33 (10), 2–5. https://doi.org/10.1029/2005GL025618.

Woor, S., Thomas, D.S.G., Parton, A., Leenman, A., 2023. Morphology and controls of the mountain-front fan systems of the Hajar Mountains, south-east Arabia. Earth Sci. Rev. 237, 104316 https://doi.org/10.1016/j.earscirev.2023.104316.

WorldClim. Historical climate data. https://www.worldclim.org/data/worldclim21.html. (Accessed 31 January 2023).

Zelenin, E., Bachmanov, D., Garipova, S., Trifonov, V., Kozhurin, A., 2022. The Active Faults of Eurasia Database (AFEAD): the ontology and design behind the continental-scale dataset. Earth System Science Data 14, 4489–4503. https://doi.org/10.5194/essd-14-4489-2022.

Zepner, L., Karrasch, P., Wiemann, F., Bernard, L., 2020. ClimateCharts.net – an interactive climate analysis web platform. International Journal of Digital Earth 14 (3), 338–356. https://doi.org/10.1080/17538947.2020.1829112.